

Auroral Illumination of Solid Bodies

Charles Loughheed Bennett¹ and Notanee Bourassa²

¹Lawrence Livermore National Laboratory

²I AM THE STORM PHOTOGRAPHY

November 21, 2022

Abstract

Numerous objects in the ionosphere, including both satellites and meteors, having rapidly varying light intensity and color have been observed in photographs taken during an active aurora. It is suggested that these variations may be attributed to Auroral Bombardment-induced Light Emission and Sputtering produced by auroral particles striking these objects. This phenomenon is found to increase the brightness of some objects by more than a thousand-fold. It is hypothesized that this phenomenon acting on a remnant dust cloud from ablated meteoric material left along the path of its trajectory through the ionosphere could produce the optical emissions known as STEVE (Strong Thermal Emission Velocity Enhancement). The July 25, 2016 STEVE event is very closely aligned in 3-dimensional direction with the location of the radiant for the Southern Delta Aquariid meteor shower. The best alignment in time with the radiant direction coincides with the appearance of rising flashes of light that occurred 5 minutes before STEVE's initial visibility. These rising flashes of light might also be caused by the hypothetical meteor.

1
2
3
4
5
6
7
8
9
10
11
12
13
14
15

Auroral Illumination of Solid Bodies

Charles L. Bennett¹ and Notanee Bourassa²

¹Retired from Lawrence Livermore National Laboratory, Livermore, CA, USA

²Saskatchewan Aurora Hunters, Saskatchewan, Canada

Corresponding author: Charles Bennett (Charlie_Bennett@comcast.net)

Key Points:

- The 3-d position and velocity vectors of numerous ionospheric objects are determined by triangulation of images from multiple cameras
- Rapid variation in color and intensity of these objects has been observed and is attributed to auroral bombardment-induced light emission
- Auroral bombardment-induced light emission of meteor dust could provide a physical mechanism for the appearance of STEVE

16 **Abstract**

17 Numerous objects in the ionosphere, including both satellites and meteors, having rapidly
18 varying light intensity and color have been observed in photographs taken during an active
19 aurora. It is suggested that these variations may be attributed to Auroral Bombardment-induced
20 Light Emission and Sputtering produced by auroral particles striking these objects. This
21 phenomenon is found to increase the brightness of some objects by more than a thousand-fold. It
22 is hypothesized that this phenomenon acting on a remnant dust cloud from ablated meteoric
23 material left along the path of its trajectory through the ionosphere could produce the optical
24 emissions known as STEVE (Strong Thermal Emission Velocity Enhancement). The July 25,
25 2016 STEVE event is very closely aligned in 3-dimensional direction with the location of the
26 radiant for the Southern Delta Aquariid meteor shower. The best alignment in time with the
27 radiant direction coincides with the appearance of rising flashes of light that occurred 5 minutes
28 before STEVE's initial visibility. These rising flashes of light might also be caused by the
29 hypothetical meteor.

30 **Plain Language Summary**

31 Most meteors emit light between 70 and 120 km above the earth from friction while passing
32 through the atmosphere. Higher altitude meteors between 130 to 170 km, where the air is too thin
33 to produce such friction, can become luminous through a different process of thermalization of
34 sputtered particles. The highest known meteor from the Orionid meteor shower became visible at
35 168 km and its light is attributed to this process.

36 In this article, we suggest that the bombardment of high-altitude solid bodies, such as space junk,
37 artificial satellites and comet or meteor dust, by concurrent auroral activity generates sufficient
38 light that otherwise invisible objects may be readily seen with widely available digital cameras.
39 We have found several examples of this process, including one meteor at a height of nearly 1,000
40 km above the earth's surface.

41 We also find that light emission along long linear trails in the ionosphere can be explained as
42 auroral bombardment-induced light emission from the remnant dust from a meteor.

43 Auroral bombardment-induced light emission of the large number of existing high-altitude
44 bodies could open up an entirely new window for a better understanding of these bodies, the
45 aurora, and the ionosphere.

46 **1 Introduction**

47 Aurora are well known to be the result of precipitating electrons or protons exciting
48 atmospheric atoms and molecules whose subsequent decay produces visible light. To the best of
49 the author's knowledge, it does not seem to have been previously noted that auroral
50 bombardment of solid bodies may produce light of sufficient intensity to be readily detected with
51 ground-based cameras and sputtered electrons of sufficient flux to be detectable in the opposite
52 hemisphere. It has been suggested by (Vinkovic, 2007) and (K.A. Hill, 2004) that meteors such
53 as those discussed in (Y. Fujiwara, 1998) and (A. Olech, 2013) too high to produce light by
54 conventional ablation processes could produce detectable light by a sputtering process, but the
55 role of the aurora as an enhancement of this process was not considered. Here evidence is
56 presented that the passage of solid objects through regions of even sub-visual auroral
57 precipitation is correlated with enhanced (sometimes by 3 orders of magnitude) visible

58 emissions. We will refer to this phenomenon as Auroral Bombardment-induced Light Emission
59 and Sputtering (ABLES). It is hypothesized that solid particles in the dust trail of a meteor or in
60 comet debris may also be illuminated by ABLES from concurrent auroral particles if the dust is
61 high enough to be exposed to auroral bombardment. One such event may have occurred on July
62 25, 2016 and this case will be the primary focus of this paper.

63 This event is one example of the thin, east-west-aligned purple-colored aurora-like
64 structure called a “proton arc” or sometimes “Steve” by auroral photographers. This event was
65 associated with sub-auroral ion drift (SAID) by (E. A. MacDonald, 2018) on the basis of data
66 from a satellite that passed over the region of this structure, and this and similar events were
67 given the backronym “Strong Thermal Emission Velocity Enhancement” (STEVE) because of
68 this correlation. The “velocity enhancement” refers to a westward ion flow in excess of 5 km/s in
69 the plasma that the satellite passed through. More recently, (W.E. Archer, 2019) has shown
70 STEVE events to be consistently associated with SAID and in the July 25 case, the Positive
71 Field-Aligned Current was measured to be approximately 500 nA/m² and extended over
72 approximately 0.7° magnetic latitude. The (D. Lummerzheim, 2001) analysis of an April 11,
73 1997 SAID event having Red-line intensity at a level similar to our July 25 event, found that the
74 positive FAC was from a flux of precipitating protons with an energy spectrum extending to at
75 least 32 keV (the upper limit of their detector). A tomographic inversion provided the altitude
76 profile of visible emissions in that case. No STEVE structures were seen in the April 11 SAID
77 event.

78 In (B. Gallardo-Lacourt, 2018) particle data was presented for a STEVE event from
79 March 28, 2008 that was crossed by the POES satellite, and these authors state “We assert that
80 such low precipitating energy fluxes (for protons and especially for electrons) cannot be
81 responsible for the luminosity observed in STEVE”. These authors, however, did not consider
82 the possible enhancement of luminosity from ABLES. In (B. Gallarod-Lacourt, 2018) a
83 statistical analysis of 28 STEVE events finds that they have a latitudinal width only ¼ the width
84 of narrow auroral structures, and typically have an equatorward displacement of about 50 km
85 over the course of an average duration of 1 hour. It is not explained how the average equatorward
86 drift velocity <0.02 km/s is compatible with the “velocity enhancement” of 5 km/s in the
87 westerly direction. It is also not explained why the latitudinal width of STEVE is so much less
88 than the auroral structures.

89 (D.M. Gillies, 2019) presents spectroscopic observations of the April 10, 2018 STEVE
90 event that reveals the green picket fence structure to be associated with a strong OI (557.7 nm)
91 emission similar to emissions produced in typical aurora. The narrow purple structure was found
92 to have a broad continuous spectrum, with some OI red-line (630 and 636 nm) emission. These
93 authors state “The above observations essentially exclude STEVE from being an auroral
94 phenomenon”. They conclude that the “elevated electron temperature” associated with the purple
95 STEVE features would produce “thermal emission” of the red-line structure.

96 (Y. Nishimura, 2019) showed that the May 8, 2016 STEVE event having a green picket
97 fence structure in photographs taken from the ground in the northern hemisphere showed a
98 conjugate structure in the southern hemisphere. These authors state “The subauroral
99 precipitation structure and upward FAC are strikingly different from typical SAID events”.
100 These authors also find that the April 12, 2008 event without a picket fence structure did not
101 show a conjugate structure in the opposite hemisphere and did not show the “strikingly different”
102 upward FAC.

103 Here we list several hitherto unanswered questions about STEVE events in general, and
104 some concerning the 2016-7-25 STEVE event in particular that we will quantitatively answer in
105 the following. Why is STEVE visible, while most SAID events are not associated with optical
106 emission? Why is the width of this STEVE (0.15° MLAT) much less than the width (1° to 2°
107 MLAT) of typical SAID events? Why is the green picket fence structure also very narrow and
108 aligned with the narrow purple streaks in magnetic latitude and longitude? Why is the green
109 picket fence at a nearly constant low altitude, while the narrow purple band initially has a linear
110 decrease in altitude along its longitudinal extent? Why are conjugate STEVE structures seen in
111 the opposite hemisphere for events with green picket fence features, but not in events without
112 these features? What accounts for the “strikingly different” upward FAC in the STEVE event
113 with a conjugate structure in the opposite hemisphere? What can account for the purple color of
114 the upper portion of STEVE? While the 7-25 SAID event displayed up to 5 km/s of westward
115 ion motion, why did this STEVE structure drift westward at a speed of no more than 0.05 km/s?

116 Our hypothesis of a remnant dust trail produced by a meteor from the Southern Delta
117 Aquariid (SDA) shower with ABLES answers all of these questions. In the following, we present
118 observational evidence that the 3-dimensional location and character of the luminosity from the
119 July 25 STEVE event can be explained by 2 components. One being the time the SDA meteor
120 struck, and the second being the location in 3-d space of the perigee of this meteor's orbit. We
121 will present observational evidence that both of these components are unambiguously
122 determined directly from the data.

123 In preparation for the discussion of our hypothesis for the July 25 STEVE event, we first
124 present observational evidence, based on the analysis of the brightness distribution in 3-d space
125 and time of several earth orbiting satellites that makes the case for the reality of ABLES, and the
126 thousand-fold gain in brightness of solid objects that can be produced by auroral bombardment.

127 In section 3 we primarily focus on the observational data. In section 4 we briefly discuss
128 the well-known phenomenon of Bombardment-induced Light Emission (BLE) and introduce our
129 Auroral BLE and Sputtering (ABLES) concept. In section 5 we turn to our hypothesis for
130 STEVE and how this hypothesis answers the questions posed in the introduction. In section 6 we
131 discuss how ABLES can provide a new window for a better understanding of the large number
132 of ionospheric solid bodies, the aurora, and the ionosphere.

133 2 July 25, 2016 Observations

134 This STEVE event was photographed by N. Bourassa from a site near Regina
135 Saskatchewan (REGI). Concurrent with the photographs published in (E. A. MacDonald, 2018),
136 a number of All Sky Imager (ASI) images were recorded, including from sites at Lucky Lake
137 (LUCK) in Saskatchewan, Athabasca (ATHA) in Alberta and The Pas (TPAS) in Manitoba. The
138 complete sequence of images from the ASI cameras are available for download from (University
139 of Calgary, 2018). The details on the spatial resolution, spectral coverage and site location for
140 these various cameras are tabulated in Table 1 in the supplemental materials.

141 To exploit parallax effects between cameras, pixels in each image were registered to local
142 angular coordinates of azimuth and altitude using a number of stars in the images. The reference
143 stars locations and magnitudes were taken from the Yale bright star catalog (Hoffleit, 2014). For
144 the REGI camera a primarily gnomonic projection (Weisstein, 2109) was used. For the ASI
145 cameras with fisheye lenses, a primarily linear equidistant projection (Bettonvil, 2005) was used.

146 For both types of lenses, correction for barrel distortion was required to provide acceptable
147 registration. The details of this process are provided in the text file, including the Matlab
148 (Mathworks, 2019) functions used, available in the supplemental materials.

149 3 Observations of satellites, meteors and STEVE

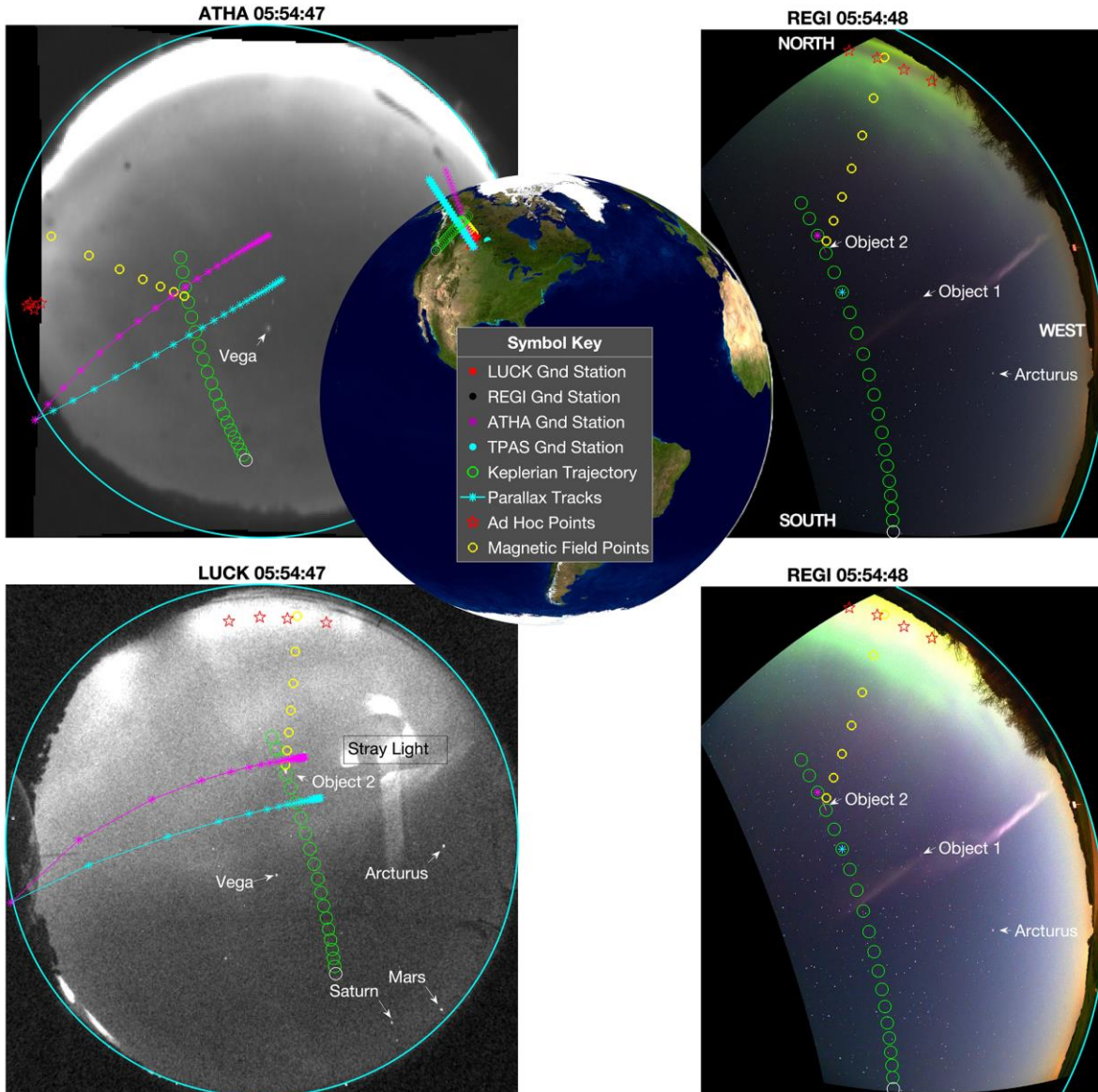
150 Within a series of REGI photographs of STEVE spanning a period of 18 minutes, 31
151 transient streak events were observed in more than 1 frame. The altitude for most of these could
152 not be determined, as no corresponding transient streak could be detected in any other ASI
153 camera by virtue of their much lower sensitivity level of approximately magnitude 3.5 for 10
154 coadded frames vs. magnitude 11 for each of the REGI RGB colors in a single frame (see Table
155 1). However, 6 of these objects were also observed in at least one frame of at least one ASI
156 camera and were determined to be high-altitude objects. These objects are numbered in terms of
157 their order of appearance. Object-6, the brightest, was seen in all 4 imagers. In addition to these
158 multi-frame objects one extended transient event was seen in a single frame in both LUCK and
159 REGI and from its brightness profile, altitude and speed is identified as a meteor.

160 A pair of transient events not included in the count of 31 above could be identified as
161 aircraft, by virtue of the regular blinking of the light at a frequency between 40 and 100 flashes
162 per minute associated with the anti-collision light system required for aircraft. One of these had a
163 color consistent with “aviation red” while the other was consistent with “aviation white”. These
164 aircraft are identified in the relevant movie files included in the supplemental materials.

165 3.1 Object-2 Example

166 Object-2 was seen by 2 of the 4 imagers over multiple successive frames. This object
167 appears as linear streaks in 20 successive REGI images at 8.34 s intervals with the locations of
168 the leading end of each streak marked by the 19 green circles and single white circle in figure 1.
169 The white circle indicates the last location of the object and direction of travel as it exits the
170 REGI camera field of view. This object also appears as shorter streaks in 6 LUCK images taken
171 at 3s intervals. The images from LUCK and REGI at the time of greatest intensity are displayed
172 in figure 1. The registered images are identified by the 4-letter abbreviation for each site,
173 together with the UTC time at the end of the exposure of the specific image. In each image, the
174 large cyan circle indicates the position of the local horizon. In all images, North is at the top and
175 West is to the right. In the LUCK image, the brightness of this object is comparable to the bright
176 stars Vega and Arcturus. This object is not detected in any of the TPAS or ATHA (grayscale)
177 images, despite the clear visibility of Vega and Arcturus in these images. The greater brightness
178 of object-2 in the LUCK image relative to TPAS and ATHA is attributed to the presence of a
179 strong spectral line in the 630 nm LUCK passband (Jun Liang, 2016) for this object.

180



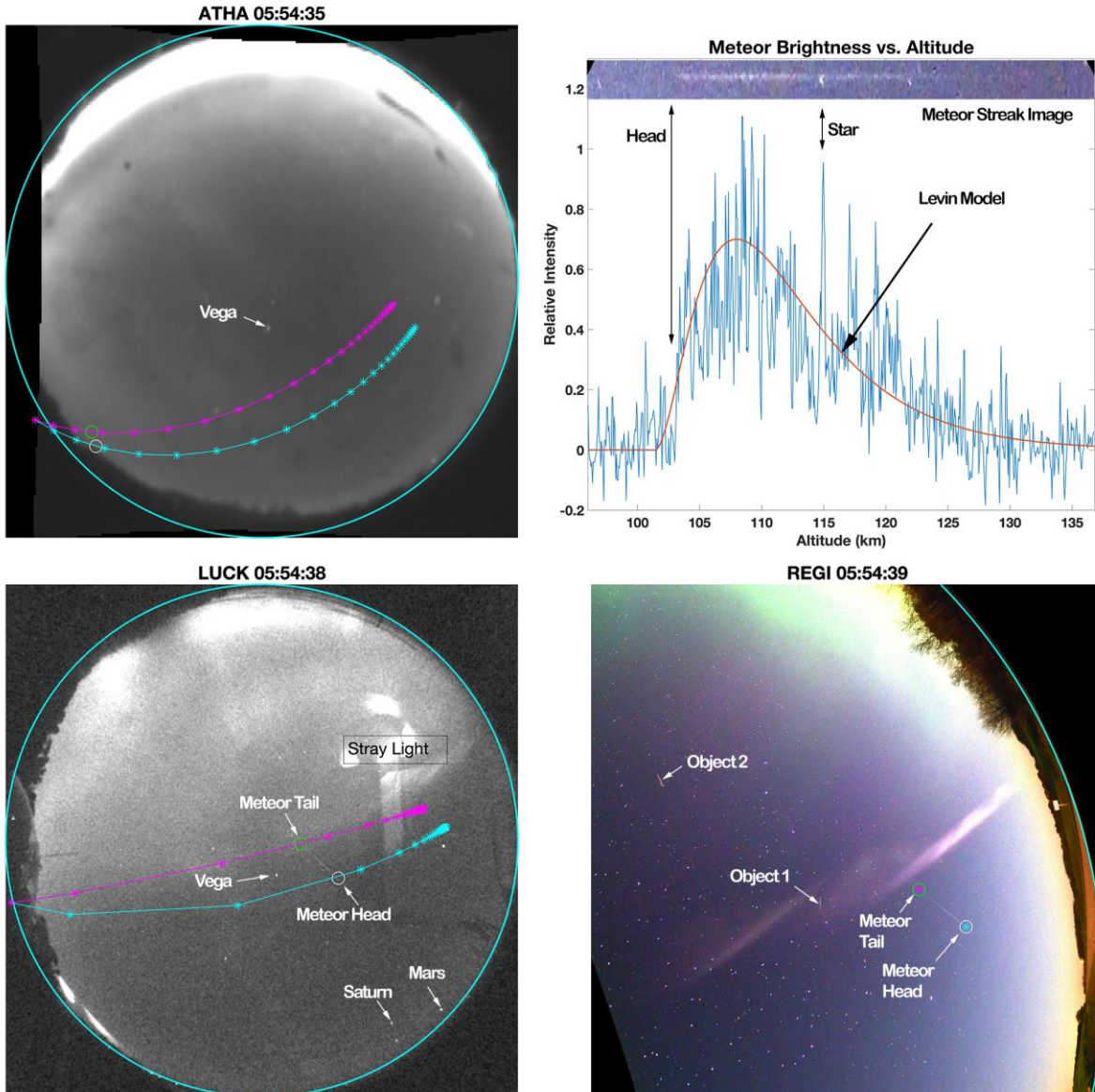
181
182 Figure 1. An example illustrating the use of parallax to determine altitude.
183

184 A particular point of interest, such as that marked by the magenta asterisk in the REGI
185 image in the center of the 3rd green circle from the top of the image, corresponds to specific
186 azimuthal and elevation angles from the REGI point of view. This particular point will appear
187 somewhere along a curve in the other imagers, with the location determined by the altitude of the
188 point. Representative locations, spaced at 100 km intervals along the line of sight extending from
189 the camera at the REGI site in the direction corresponding to the magenta asterisk in the REGI
190 image, are indicated by the magenta asterisks shown superimposed on the images from the other
191 imagers, as well as over the surface of the globe at the center of the figure. These are labeled
192 “Parallax Tracks”. The magenta asterisks in each image are joined by magenta line segments.
193 The altitude of the magenta asterisk point in the REGI image is determined by the intersection of
194 the magenta parallax track with the observed trajectory of object 2 in the LUCK image.

195 Similarly, the cyan asterisks linked by cyan line segments represent the line of sight
196 corresponding to the center of the 6th green circle from the top in the REGI image. Just as for the
197 magenta case, the altitude of the cyan asterisk in the REGI image is determined by the
198 intersection of the cyan parallax track with the trajectory seen in the LUCK imager. Parallax
199 tracks are extremely helpful in the process of altitude determination but for clarity are not always
200 shown in later figures.

201 Synchronization of the REGI and LUCK clocks can be obtained from the position of the
202 light streaks seen in both imagers. As the leading end of the object 2 streak is approximately 1/8
203 of the inter-circle distance above the center of the 4th green circle in the LUCK image, the
204 exposure of the LUCK image shown terminated approximately 1 s before the exposure of the
205 REGI image shown. The LUCK recorded times were taken as the reference. The REGI times as
206 recorded in the metadata for each photograph needed to be adjusted by subtraction of 163
207 seconds. The ATHA recorded times required subtraction of 24 seconds, while the TPAS
208 recorded times required subtraction of 14 seconds. With the altitude of the green circles between
209 the magenta and cyan parallax tracks determined, the 3-dimensional position and velocity
210 vectors can be determined using any pair of successive points. It is found that all 20 of the REGI
211 positions along the trajectory of object-2 are consistent with a Keplerian orbit, having an altitude
212 at the magenta point of 737 km, and a speed of 9.0 km/s. As this speed is significantly less than
213 the escape velocity for this altitude of 10.3 km/s, this object is in a gravitationally bound orbit
214 about the earth, and thus this object is identified as a satellite in Low Earth Orbit (LEO). The
215 rotation of the earth underneath the Keplerian trajectory must be accounted for in order to yield
216 the correct positions in the other REGI images.

217 Four “Ad Hoc” points marked by red pentagrams along the distinct edge of the green
218 aurora at the northern end of the REGI image (best seen in the REGI image in the upper right
219 hand corner of the figure displayed with an expanded intensity range) are used to determine the
220 magnetic latitude of that aurora as discussed further in section 3.5 below. The magnetic field was
221 computed with the POMME code (CIRES, 2019) using parameters reflecting the state of the
222 magnetosphere at the time of the image. The specific magnetic field line that passes through the
223 trajectory of Object-2 near its point of greatest brightness is shown by the series of yellow
224 circles. The circles mark points along the magnetic field line at altitudes in steps of 100 km along
225 the field line starting from 100 km up to 700 km. It is found that the field line passing through
226 the trajectory of Object-2 at its brightest position also passes through the auroral sheet marked by
227 the red pentagrams.



228
229 Figure 2. An example illustrating the use of parallax to determine meteor trajectory.

230 **3.2 Meteor Case**

231 The LUCK and REGI images shown in figure 2 show an example of a single frame
 232 transient event. The brightness of this object varies along its length just as expected for a typical
 233 unfragmented meteor. In the upper right corner of figure 2, the plot of the grayscale brightness of
 234 this meteor extracted from the REGI image is compared to the model of (Levin, 1963) for the
 235 case of a spherical body shown by the red curve. In the top portion of this plot, the region of the
 236 REGI image containing this meteor is shown in a narrow strip that is aligned with the intensity
 237 plot immediately below it, with arrows indicating the position of a star that happened to lie along
 238 the meteor streak. Since the meteor trail extends the full distance between the parallax tracks
 239 superimposed on the LUCK image, it can be concluded that the meteor light occurred entirely
 240 within the 2 s LUCK camera exposure. This allows a lower bound of 20.3 km/s to be placed on
 241 the meteor speed.

242 In the REGI image shown, objects-1, -2, and the meteor are all simultaneously visible,
243 with an enormously large range of altitudes. The conventional approach of mapping ASI data to
244 a single altitude is hopelessly inadequate for the analysis of such images. In contrast, the
245 approach described here involving the use of “parallax tracks” works quite well, provided clear
246 points of interest can be identified in nearly simultaneous images taken from at least 2 sites at
247 different locations.

248 3.3 Brightness Variations of Streaks as a Function of Time and Position

249 For both object-1 and object-2 the observed streaks in the REGI images are spread out by
250 their motion over approximately 130 pixels in the original photographs. By virtue of the high
251 resolution and high signal to noise ratio of the REGI data, the variation of the observed intensity
252 along the length of the individual streaks of light in each REGI frame can be usefully converted
253 to a variation as a function of time. The single pixel temporal width obtained is approximately
254 30ms. The time varying intensities for each of the 3 colors in the REGI data are plotted in the
255 upper section of figure 3. The width of the peaks corresponds to the 4 s exposure for each frame,
256 while the spacing of peaks corresponds to the 8.34 s period between frames. The observed
257 intensities were converted to apparent magnitude using known stars as references. One example
258 is the star β Corona Borealis shown in the small vignette taken from the frame corresponding to
259 the greatest observed intensity for object-1 as indicated by the double arrow. The tilted donut
260 shape of the star image is typical of the stars seen in this portion of this particular photograph and
261 is due to a lack of perfect focus in this image. This blurring also reduces the temporal resolution
262 and is the reason for the slanted edge of the streak at either of its ends. At its brightest, object-1 is
263 over 1,000 times brighter than the threshold of detection at the background level.

264 The rapid variations in intensity and color observed for both object-1 and object-2 are not
265 consistent with blackbody thermal emission. They may be consistent with ABLES, as will be
266 discussed further below.

267 The brightness of all 6 objects are displayed as a function of magnetic latitude in the
268 lower left of figure 3. The relative brightness along the trajectory for each object is indicated by
269 the relative sizes of the circles in the lower right. The circle centers correspond to the locations of
270 the leading end of each streak in successive images. The Keplerian orbital parameters that best fit
271 the observations of each object are shown in the legend. Object-1 was observed in 24 REGI
272 frames, but not in either ATHA or TPAS. There were 2 possible streaks seen in 2 different
273 LUCK frames corresponding to 2 different altitudes, and it is also possible that it was low
274 enough to be below the horizon in the other imagers, so its actual altitude is uncertain.
275 Nonetheless, the estimated magnetic latitude distribution shown for object-1, based on the
276 assumption of an altitude of 700km is probably good to within 1° regardless of its exact altitude.
277 Object-3 was observed in 28 REGI frames for one pointing of the camera, and in an additional
278 24 frames for a second pointing of the camera. It was also observed in ATHA for over 40 frames.
279 Object-4 was observed in 10 REGI frames, but only a single LUCK frame. Thus only a single
280 altitude can be determined, but the slope of this object’s trajectory cannot be determined, so its
281 speed is uncertain. Object-5 was observed in 9 REGI frames for one pointing of the camera, and
282 in an additional pair of REGI observations (the northernmost 2 points in the plot) for a different
283 pointing. Object-5 was seen in 63 TPAS frames spanning a greater time range than the REGI
284 observations but was not seen in ATHA and was only seen in LUCK for 22 frames. Object-6 was
285 seen in 50 TPAS frames and 34 REGI frames (at 2 second intervals from the REGI.MOV
286 frames). It is also seen in 18 ATHA frames and 28 LUCK frames. The plotted circles for object-

287 6 were at 3 s intervals, as it was seen over the longest period of time in the TPAS imager. The
288 brightness for all other objects plotted were taken from the REGI imager at 8.34 s intervals. In all
289 cases, the intensities plotted have been corrected for the effects of range assuming an inverse
290 square law, so that a constant brightness would plot at a constant level independent of range.

291 The peak brightness of object-2 coincides with its crossing the auroral sheet located at
292 62° magnetic latitude and whose lower edge is indicated in figure 1 by the 4 red pentagrams. In
293 contrast, no other object has such a peak in brightness as it crosses this same region of magnetic
294 latitude. Objects -1, -4 and -6 instead have brightness peaks at $58.5^\circ \pm 1^\circ$, while object-2 also
295 shows a weak secondary peak in brightness near there while its brightness is too low to be
296 detectable between 58° and 60.6° . Object-4 is not even detectable at 62° , despite being well
297 within the field of view of the REGI camera. Objects -3 and -5 do not have brightness peaks
298 within the field of view of the REGI camera. Also, despite being well within the field of view of
299 the REGI and/or ASI cameras, objects -2, -4 and -6 have a brightness too low to be detected at
300 latitudes below 56° .

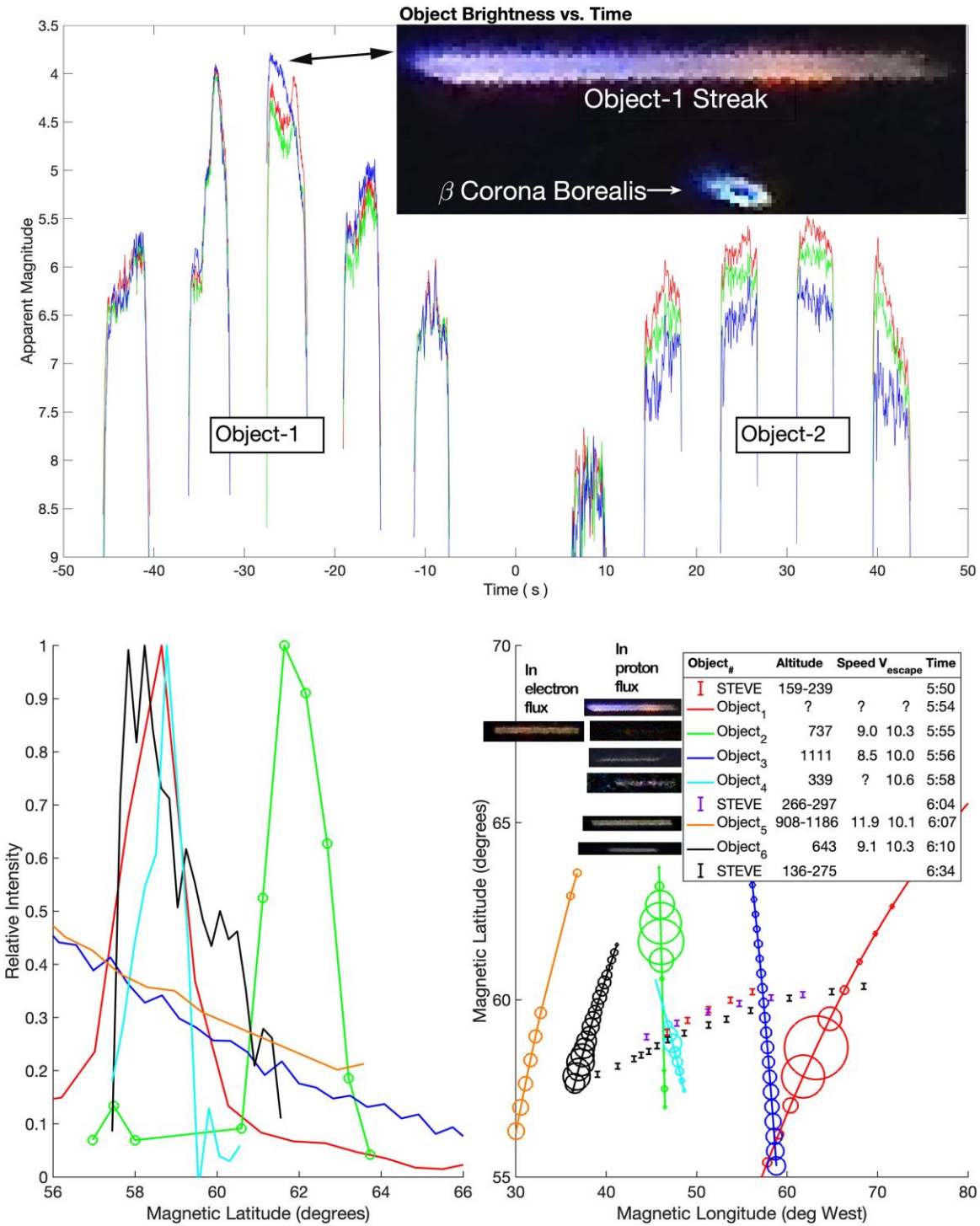
301 The brightness peak near 62° in magnetic latitude is clearly associated with the electron
302 aurora seen simultaneously in the REGI photographs. The brightness peak at 58.5° , on the other
303 hand, has no significant visible manifestation in the REGI photographs. It is thus most probably
304 the result of a secondary peak in the sub-auroral proton flux of much less intensity than the
305 concurrent super-auroral proton flux observed in the FESO data. This presumed distribution of
306 proton and electron fluxes is similar to that observed in the proton auroral event discussed by (D.
307 Lummerzheim, 2001) in which Tomographic Imaging was done and an altitude profile of
308 emissions along a magnetic meridian was extracted. In the Lummerzheim work, the 2:45 pass of
309 the DMSP satellite revealed a strong proton flux poleward of the primary electron flux, with a
310 weaker proton flux peak equatorward of the primary electron flux. This electron and proton flux
311 distribution is apparently similar to that seen on July 25, 2016.

312 The 1.5° width of the brightness peak at 58.5° in figure 3 is typical of the width and
313 location of SAID events (E. Mishin, 2017). In our data, the existence of this sub-auroral proton
314 flux is revealed by the sensitivity “magnification” provided by ABLES acting on objects passing
315 through the region of proton bombardment.

316 In the legend for the plots in the lower half of the figure, vignettes for all 6 objects are
317 shown to the left of each objects’ respective entry. The right column of vignettes corresponds to
318 the appearance of the objects while they are within the proton flux region. The left-hand vignette
319 column has a single row corresponding to the appearance of object-2 in the electron flux region.

320 Also shown in the lower right of figure 3 are 3 examples of the location of STEVE
321 ranging from the earliest to the latest times for which concurrent REGI, LUCK and ATHA data
322 are available. The latitudinal distribution of STEVE is confined to the same region as the sub-
323 auroral proton flux. The width of the bars shown for STEVE are not uncertainties in position but
324 rather represent the latitudinal width 0.15° of the observed light distribution at any given
325 longitude. This width is an order of magnitude narrower than the latitudinal width of typical
326 SAID events. The drift in the STEVE location over the course of time could be entirely
327 southward, entirely westward, or a mixture of both. Between 5:50 and 6:34 if the location of
328 STEVE seen in figure 3 is associated with an equatorward drift rather than a westward drift, the
329 latitude decreases by approximately 0.37° in 44 minutes. This corresponds to a speed of no more
330 than 20 m/s in the latitudinal direction. On the other hand, if the drift is purely westward, the
331 longitudinal location changes approximately 5° in 44 minutes corresponding to a drift speed of
332 approximately 100 m/s in the longitudinal direction. This later speed is roughly that of the

333 neutral wind speeds discussed by (G. Liu, 2013), but it is nearly 2 orders of magnitude less than
 334 the 5 m/s SAID flow speed measured by (E. A. MacDonald, 2018).



335
 336 Figure 3. Object brightness is plotted as a function of time (upper half) and location (lower half) in this figure. The
 337 location of STEVE emission is plotted with error bars representing the width of the observed emission.

338 3.4 Object Identifications

339 Objects -2, -3 and -6 are identified as satellites, as their speeds are less than the escape
340 velocity for their measured altitudes. As the speed of object-5 was greater than the escape
341 velocity this object is identified as a meteor. Because of the uncertainty in its altitude and speed,
342 object-1 cannot be identified as either a meteor or satellite. Because of the uncertainty in its
343 speed, object-4 cannot be identified as either a meteor or satellite. Object-3 is tentatively
344 identified as NORAD satellite number 25876, based on the proximity in space and time of the
345 Keplerian orbit computed from the archived orbital elements from (Kelso, 2019) to the observed
346 trajectory.

347 The object discussed in figure 2 has a brightness distribution entirely consistent with a
348 typical meteor trail. Because it is seen in only a single frame in both the LUCK and REGI
349 cameras, only a lower bound on its speed of 20.3 km/s can be derived. As its speed is above the
350 escape velocity, and its intensity distribution appears meteoric, it is identified as a meteor. In the
351 3600 LUCK frames between 5:00 and 8:00, this is the only conventional meteor trail found. It
352 may not be merely coincidence that this meteor trail happens to lie within the $58.5^{\circ} \pm 1^{\circ}$ region
353 corresponding to the lower latitude brightness peak. It could be that its luminosity was enhanced
354 by ABLES.

355 3.5 Auroral Imaging Case and Magnetic Field Line Identification

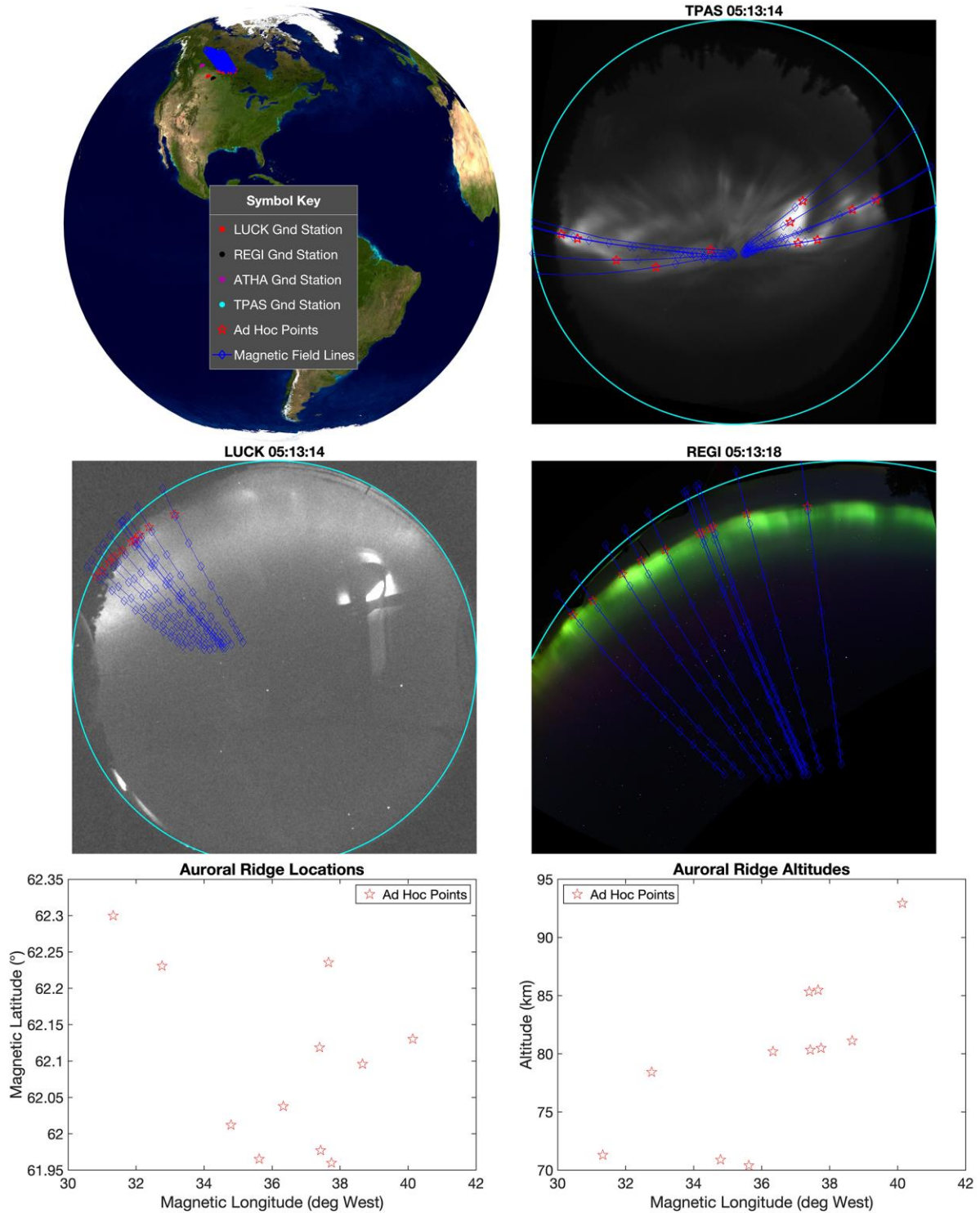
356 An example of the 3-dimensional analysis of auroral features is shown in figure 4. Here a
357 series of 11 “Ad Hoc” points indicated by red pentagram markers are chosen along the ridge of
358 the very bright auroral structure visible in the TPAS image shown. The displayed intensity range
359 for the TPAS image is chosen to avoid saturation in the image. In the REGI image of this auroral
360 activity, the lower edge of the aurora is quite clear cut, and a precise altitude for the pentagram
361 points can be determined by comparison of the REGI and TPAS images. The altitudes and
362 locations for the 11 points are indicated in the bottom of the figure.

363 Magnetic field lines passing through each of these points are shown in the figure by blue
364 lines with diamond milestones at altitude intervals of 100 km. The magnetic field lines shown
365 start from a geodetic altitude of 0 km and extend to a maximum altitude of 1,000 km. The
366 POMME code values for the magnetic field are valid to at least 2,000 km in altitude, and well
367 beyond the 1,000 maximum altitude shown here. Note that the positions of the red pentagrams
368 relative to the 100 km altitude milestones along the various magnetic field lines vary as expected
369 for the general increase in the altitude of the edge of the aurora going from east to west across
370 the image.

371 At the time of this data, the aurora was almost directly over the TPAS imager, and the
372 point of view is staring almost directly up along the local magnetic field lines indicated. The
373 “thickness” of the sheet of auroral activity can be most clearly seen from this end-on perspective,
374 and it is found in places to be only 2 km even while extending over 100km in altitude. A rather
375 complex structure of folds is seen. This structure is dynamic, varying significantly from minute
376 to minute, although the minimum altitude doesn’t vary significantly on this time scale.

377 The REGI image shows that the green auroral fine structure is closely aligned with the
378 magnetic field lines. This is most clearly seen at the eastern side, with smaller linear structures
379 appearing within the overall green band. The green auroral structure seen in the REGI image is
380 presumably produced by precipitating electrons. From the altitude of the bottom of the green
381 emission it seems that the electron energies were approximately at the 10 keV level, based on
382 typical auroral transport models (Solomon, 2001), but with a significant variation in the energy

383 of the precipitating particles along the edge of the auroral structure based on the variation in
 384 minimum altitude. At the time of this image, with the triangulation of the red pentagram points,
 385 the magnetic field lines lead to a value for the magnetic latitude of the green auroral features of
 386 $62.15^\circ \pm 0.20^\circ$. Over time, the latitude of the green auroral features is seen to vary somewhat.



387 Figure 4. The auroral structure is illustrated.
 388

389 In order to account for the variation in magnetic latitude of the electron aurora, in images
390 containing visible green auroral sheets, but without a corresponding view from a second site to
391 determine the altitude, it was assumed that the lower edge of the auroral sheets was at the mean
392 altitude determined in figure 4. As an example, the red pentagram “Ad Hoc” points shown in
393 figure 1 were taken to have altitudes of 80 ± 10 km, corresponding to the altitude range of the
394 auroral edge observed found for figure 4. With this altitude range, it was found that the magnetic
395 latitude of the green auroral feature at the time shown in figure 1 was approximately $61.8^\circ\pm 0.3^\circ$.
396 This is consistent with the location of the brightness peak seen for object-2 as shown in figure 3.

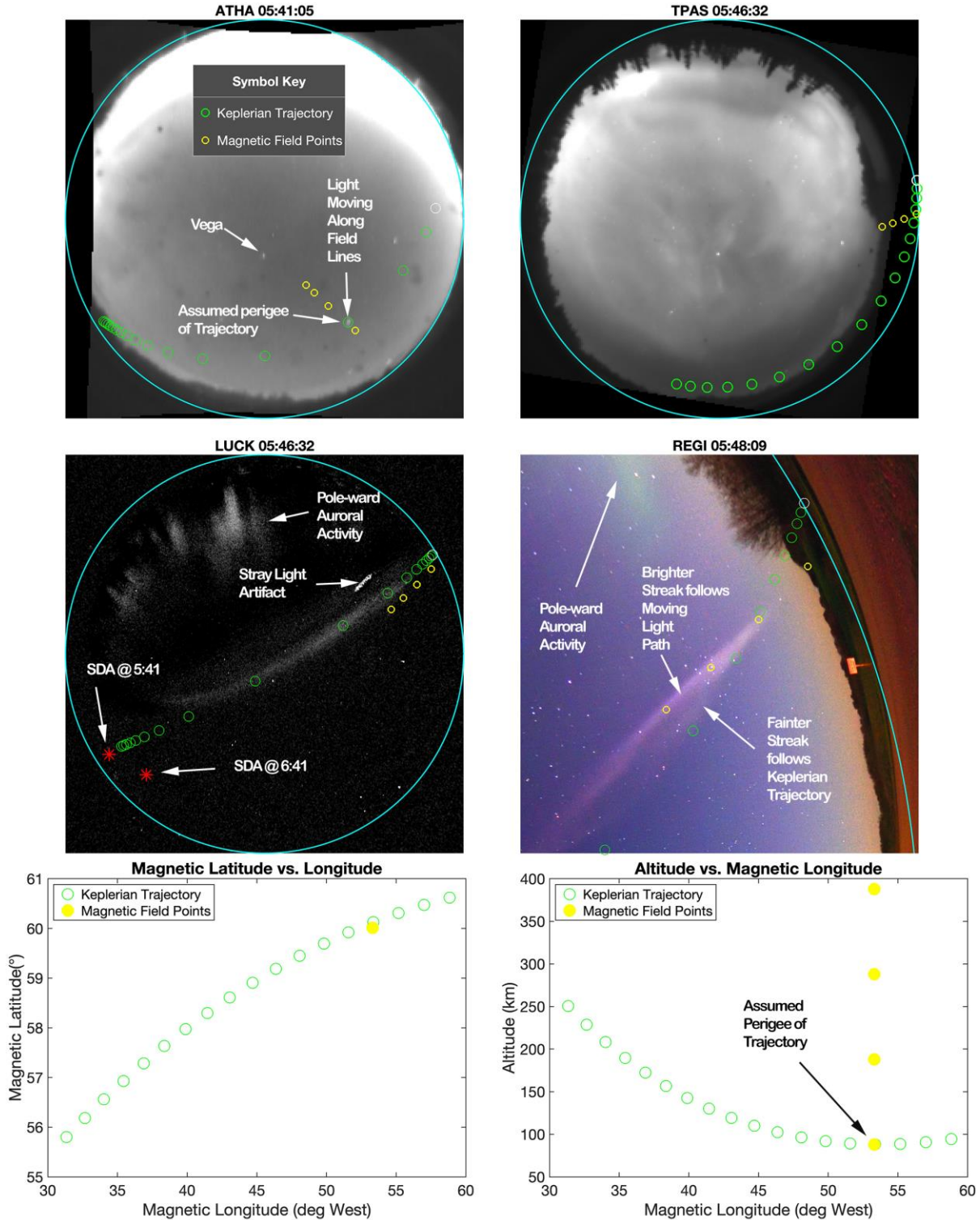
397 3.6 STEVE

398 The earliest appearance of STEVE is best shown by the difference image of the LUCK
399 data shown in the figure 5. Here, to enhance contrast, 20 images spanning 5:46:32 to 5:47:29
400 were coadded and the sum of 20 images spanning 5:45:32 to 5:46:29 subtracted. This time
401 corresponds to the earliest onset of STEVE and reveals a highly linear structure that points
402 toward the radiant indicated by the red asterisk (labeled SDA@5:41) for the Southern Delta
403 Aquariid (SDA) meteor shower that was going on at the time. The position of the SDA radiant an
404 hour later is indicated by the second red asterisk (labeled SDA@6:41). The alignment of the
405 linear structure with the SDA@5:41 direction in 3-dimensions is confirmed by the fact that the
406 Keplerian trajectory aligned with this structure asymptotically approaches the location of the
407 SDA@5:41 point in the LUCK image.

408 At 5:41 a moving light is seen in the ATHA data. The motion of this light can be seen in
409 one of the movies in the supplemental materials. In this movie the trajectory of an object
410 following a Keplerian trajectory is superposed for context. The motion of the moving light
411 approximately follows the local magnetic field lines indicated by the 4 yellow magnetic field
412 points whose coordinates are shown in the lower plots. These same 4 magnetic field points are
413 also shown in one of the movies. The Keplerian trajectory shown is assumed to have its perigee
414 at the location of the earliest appearance of the moving lights in the ATHA camera data as
415 indicated in figure 5. The speed for this trajectory is assumed to be 42 km/s as typical for SDA
416 meteors. The direction of the trajectory at perigee is determined by requiring alignment with the
417 direction to the SDA radiant in 3-d space at 5:41. The altitude at perigee is determined using the
418 earliest available REGI image in conjunction with the 5:41 ATHA image shown.

419 The earliest available REGI image at 5:48:09 showing STEVE was taken 97 seconds
420 after the 5:46:32 LUCK image. The light seen in the ATHA images to be moving up along the
421 magnetic field lines appears to have left a luminous residue of sufficient intensity to be seen in
422 this REGI image, but not in the 5:46 LUCK, ATHA or TPAS images. This luminous residue is
423 seen in the REGI images to gradually fade over the next several minutes, but to not significantly
424 change in location. By identifying this luminous streak at 5:48 with residue from the moving
425 light seen in the ATHA data at 5:41 that is made visible in REGI by ABLES, the location of the
426 magnetic footprint coordinates of the yellow circles are determined, as well as the altitude of the
427 perigee of the Keplerian trajectory. The yellow circles indicating points along this particular
428 magnetic field line are seen to closely follow the bright streak in the REGI image. The green
429 circles indicating the 3-d Keplerian trajectory shown are at 2.5 s time intervals. That the brighter
430 streak along the magnetic field lines in the REGI image is not seen in the LUCK image can be
431 attributed to the lack of significant line emission at 630 nm from the luminous residue at this
432 time.

433 With the perigee chosen to lie at 53° W magnetic longitude, coinciding with the longitude
 434 of the moving lights, its altitude is found to be 88 km. If the perigee is instead assumed to be a
 435 slightly smaller 50° W value, then the altitude at perigee becomes 112 km. Slight changes in the
 436 location of the perigee don't significantly change our analysis aside from the perigee altitude.
 437



438
 439 Figure 5. The 3-dimensional structure of the earliest STEVE emission is quantified by parallax analysis.

440

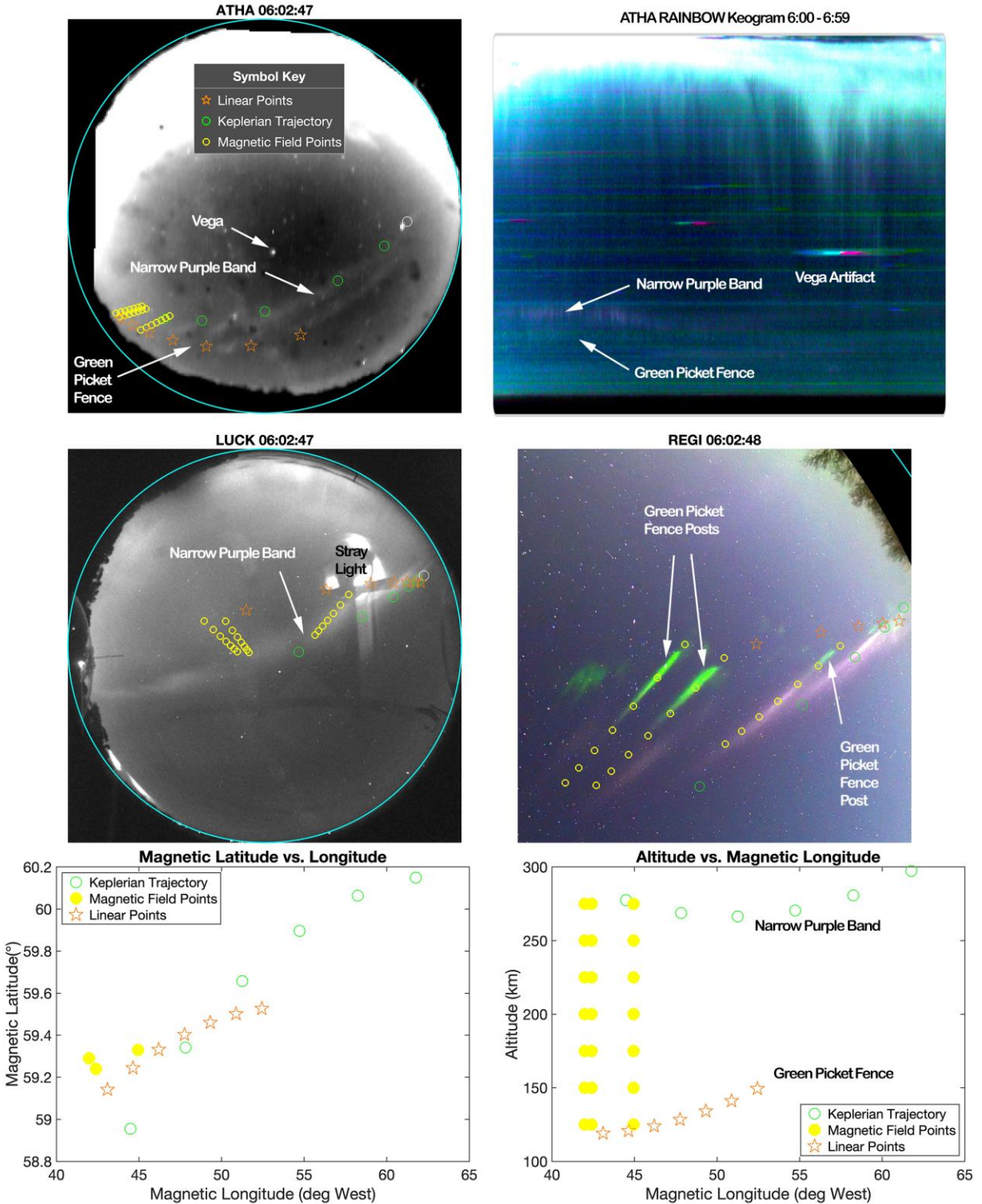
441 As soon as STEVE appears in the ATHA imager it is apparent from the movie file
442 showing grayscale ATHA data in the supplemental materials that there are 2 distinct bands of
443 luminosity. The full color (B.J. Jackel, 2014) ATHA keogram spanning the 6:00 to 6:59 time
444 interval displayed in figure 6 confirms the difference in color seen far more clearly in the REGI
445 image between the upper and lower structures. The vertical scale of the keogram is displayed so
446 that it conforms to the vertical extent of the grayscale ATHA image to the left. Here 10
447 successive frames of LUCK data and 5 frames of the grayscale ATHA data have been co-added
448 to improve the signal to noise ratio for the ASI images. As Vega passes across the center of the
449 ATHA imager it produces the rainbow-colored streak artifact seen near 6:45 in the keogram. In
450 the keogram spanning the 6:00 to 6:59 time interval, it is seen that the lower band has a greenish
451 tinge, while the upper band has a purple hue. In the REGI image at 6:02:48, 3 distinct “green
452 picket fence posts” are indicated. Magnetic field lines corresponding to the location of these 3
453 posts are shown by the series of yellow circles. For some posts, such as the western-most
454 exemplar case shown in the figure, there is continuity between the green tip and a higher-altitude
455 purple streak. For other posts, there is either a gap between the green tip and higher-altitude
456 purple streaks, or no corresponding co-linear purple streak visible. For some cases there are field
457 aligned purple streaks but no collinear green streak. Examples of all of these possibilities can be
458 seen in the 6:02:48 REGI image.

459 In the REGI movies in the supplemental materials, a much larger number of green picket
460 fence post examples can be seen. The motion of each of the Objects -1 through -6 can be seen in
461 these movies, together with additional transient streaks labeled with letters. The numerous
462 transient events not detectable in the other ASI data sets because of their lower sensitivity are
463 most likely satellites, but without a confirmation of altitude this cannot easily be confirmed.
464 Several frames in the REGI movies exhibit a transient diffuse green glow that is occasionally
465 observed. A few transient events are observed to blink regularly and are identified as aircraft
466 with flashing collision avoidance lights. A few single frame streaks are identified as conventional
467 meteors based on their appearance.

468 A straight line running approximately through the lower altitude extreme of the picket
469 fence posts in figure 6 is indicated by the 7 orange pentagrams evenly spaced along the line. This
470 straight line runs through the lower band labeled “Green Picket Fence” in the ATHA image and
471 keogram. The green structures are not visible in the LUCK imager as they have little intensity in
472 the narrow 630 nm band. The “Narrow Purple Band” indicated by the points along the
473 “Keplerian Trajectory” is at a distinctly higher altitude than when it first appeared, although its
474 magnetic coordinates have not changed significantly, as can be seen in figure 3. The location of
475 the “Narrow Purple Band” at the latest time 6:34 that it is seen significantly in both LUCK and
476 ATHA has not significantly further changed in altitude but has apparently drifted a bit southward
477 or possibly westward.

478 As best seen in the ATHA movie from the supplemental materials, blobs of relatively
479 brighter luminosity in the upper and lower bands are observed to move in a coordinated fashion,
480 so that a typical upper and lower blob in an associated pair lie along a common magnetic field
481 line. These field lines appear approximately as “radial bicycle spokes” (such as the field lines
482 indicated in figure 6 by the yellow circles) that are moving about the center of the ATHA image
483 movie. Although it is somewhat difficult to be precise, considering the “fuzziness” of the blobs,
484 it was found that the *apparent* velocity for blobs in the upper band was initially directed
485 downwards along the band at a speed of several km/s. In contrast, the *apparent* velocity for blobs

486 in the lower band was directed horizontally along the band at a speed of somewhat less than the
487 speed in the upper band. These speeds are comparable to the westerly ion speed seen by
488 SWARM (E. A. MacDonald, 2018). It seems highly unlikely that there are actual physical blobs
489 of luminous material descending at such a rapid speed along the upper inclined STEVE band. It
490 is also highly implausible for there to be a population of lower altitude blobs that just happen to
491 move at a speed such that they remain on the same magnetic field lines as their higher altitude
492 partners! The resolution of this apparently paradoxical appearance is explained below.

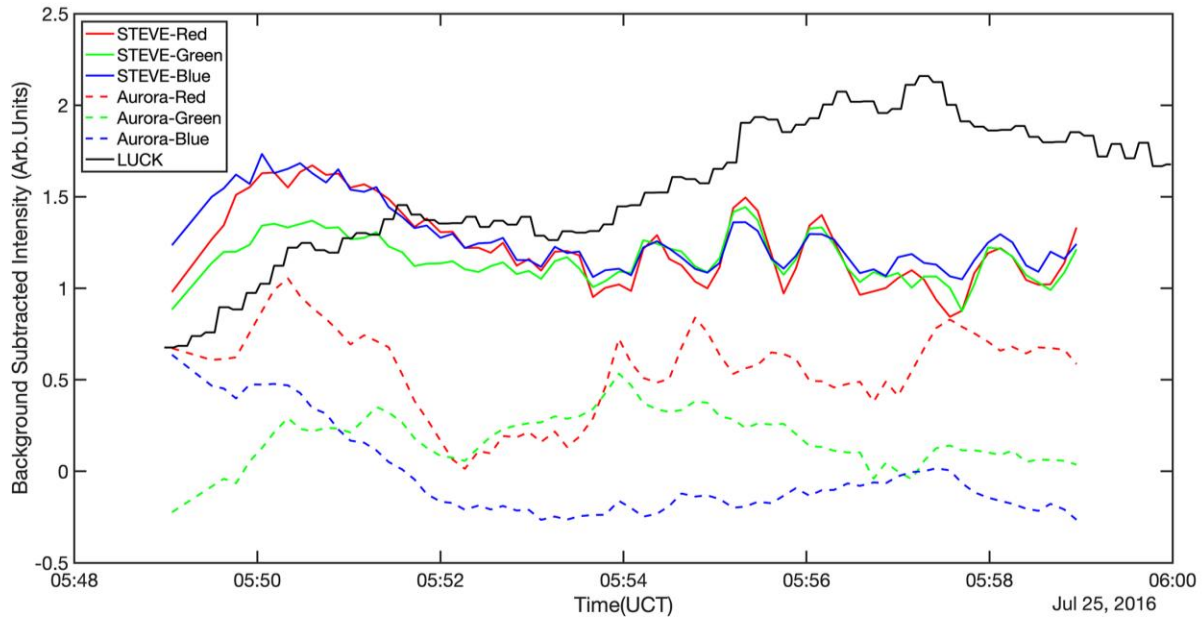


493
 494 Figure 6. The 3-dimensional structure of the Green Picket Fence is quantified by parallax analysis.

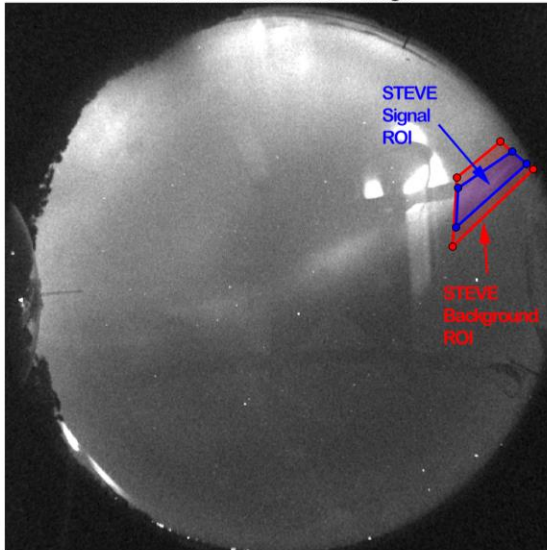
495 **3.8 STEVE Pulsations**

496 It is found that the intensity of the STEVE emission is, in certain places, pulsating with a
 497 period of about 1 minute, as shown in figure 7. In this figure, the integral intensity within the

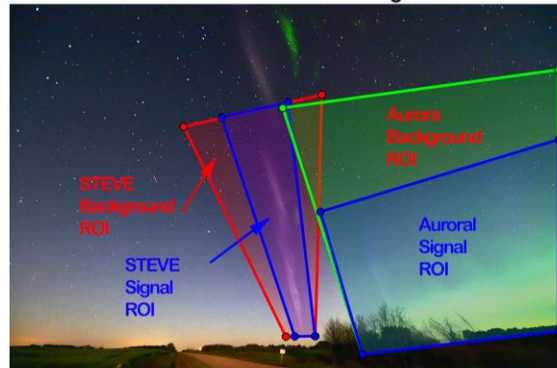
498 Region of Interest (ROI) shown in blue for the signal is corrected by the subtraction of the
 499 average background per pixel determined in the red ROI. A similar procedure is used for an
 500 estimation of the intensity within the electron aurora appearing to the north of STEVE, except
 501 that the Aurora result plotted has a linear background subtracted for each color and also an
 502 arbitrary linear scaling applied for convenience of display in the plot.



LUCK ROI Selection Image



REGI ROI Selection Image



503 Figure 7. Pulsations in the luminosity of STEVE emission in the indicated ROIs is plotted in the upper graph. The
 504 lower images show the boundaries of the ROIs used.
 505
 506

507 Weaker pulsations at this same period are observed in the 630 nm LUCK data. The
 508 STEVE pulsations are apparent in the playback of the supplemental movie in the (E. A.
 509 MacDonald, 2018) reference. It can also be noticed that the pulsations in STEVE are correlated
 510 with the much weaker pulsations in the electron aurora seen to the north. The pulsations in

511 STEVE appear to be approximately 180° out of phase with respect to the electron auroral
512 pulsations.

513 The period of STEVE pulsations appears to be unusually long compared to the normal
514 range 2-20 s of auroral pulsations (Johnstone, 1978). The period seen here cannot be long
515 because of an aliasing artifact, as it is seen in both REGI data with an 8.4 s sampling interval and
516 LUCK with a 3 s sampling interval. The long period also does not seem to be associated with the
517 larger “off” and shorter “on” times associated with long period pulsating aurora (Yamamoto,
518 1988), as the intensities appear to be nearly sinusoidal while fluctuating.

519 Although the STEVE pulsation period is unusually long, the fact that it is so highly
520 correlated with the electron auroral pulsations indicates that the narrow purple band structure of
521 STEVE is energized by auroral activity and is not solely an ionospheric phenomenon.

522 4 Bombardment-induced Light Emission

523 According to (Thomas, 1979) “An inescapable consequence of the bombardment of a
524 solid with atomic particles in the energy range above a few tens of electron volts is the emission
525 of particles from the solid via sputtering. A fraction of the sputtered flux emerges from the solid
526 surface in an electronically excited state and gives rise to the emission of light in a volume
527 outside the surface”. This phenomenon is known as Bombardment-induced Light Emission
528 (BLE). As the energy of auroral particles is well above this threshold, it is to be expected that
529 upon encountering solid bodies, such as those identified as objects-1 through -6, substantial light
530 emission will take place.

531 Although BLE of solids is a general phenomenon occurring in a wide variety of
532 materials, sputtering by electrons seems to be much more sensitive to the material composition
533 (Townsend, 2005). We will refer to Auroral BLE, whether by electrons or ions and whether by
534 trapped or precipitating particles as ABLES.

535 ABLES can account for the rapid variations in the observed light intensity shown in
536 figure 3, especially object-1. With the assumption that the object is tumbling as it passes through
537 the region of auroral bombardment, and that as different materials are exposed to the auroral
538 bombardment, the nature of the emitted spectrum and its intensity will change accordingly.

539 The spectrum of the emitted light will depend on the nature and energy of the
540 bombarding particles, as well as on the material composition of the solid body. It appears, for
541 example, that the composition of object-2 was more readily illuminated by the electron flux than
542 the proton flux, based on its much lower observed brightness for the lower latitude points. It is
543 suggestive that portions of the object-1 streak in figure 3 resemble the color of STEVE seen at
544 the same time and in the same photograph.

545 5 STEVE hypothesis and answers to questions

546 Our hypothesis is that STEVE emission in general could be produced by ABLES of solid
547 material, i.e. dust, left behind by the passage of a meteor at some time prior to the first
548 appearance of STEVE. The remnant debris would initially lie along the trajectory of the meteor.
549 From the estimate of the 7-25 meteor’s trajectory, it would have passed almost directly over the
550 REGI location. Even though there is no photographic evidence to confirm or deny the existence
551 of this meteor at the time of its passage, N. Bourassa would have certainly noticed a *normal*
552 meteor passing across the entire sky but did not, and no such visible meteor trail appears in any
553 of his photographs. The ATHA 5:41 flashes would have been only barely above the REGI
554 horizon and would plausibly not have been noticed by N. Bourassa. The perigee of this

555 hypothetical meteor must have been at sufficiently high altitude that ablative heating did not
556 produce sufficient luminosity for the meteor to be noticed from the ground or detectable in the
557 ASI cameras. On the other hand, the perigee of the hypothetical meteor must have been at
558 sufficiently low altitude to produce an extended trail of dust. The estimated altitude of the
559 perigee described in section 3.6 does indeed lie near the threshold between normally visible and
560 normally invisible meteors (Plane, 2012).

561 In the absence of bombardment by auroral particles, this debris would remain nearly
562 invisible, as is found to be the case for all 6 objects shown in figure 3 over the portions of their
563 trajectories significantly poleward of the auroral region of bombardment. Just as a laser beam in
564 air may only become visible upon passage through a region of smoke or dust, STEVE emission
565 could become visible only where both remnant dust and auroral bombardment coexist. The
566 narrow width of STEVE emission relative to SAID events is explained by the narrow width of
567 the dust distribution. The green picket fence features could also be produced by secondary
568 electrons from the sputtering of remnant material that continue to travel down along field lines,
569 producing typical auroral emissions in collisions with the lower atmosphere. That secondary
570 electrons would be constrained by the local field lines explains the co-location of the green
571 picket fence with the higher altitude narrow purple bands in STEVE in magnetic coordinates. It
572 appears that a population of sputtered ions (not necessarily as tightly constrained as the sputtered
573 electrons to magnetic field lines because of multiple charge exchange collisions) could perhaps
574 be responsible for the very diffuse glow most clearly seen in the last frame of one of the REGI
575 movie in the supplemental materials. In the event of insufficient sputtered intensity, the picket
576 fence would not be detectable. The picket fence is at nearly constant altitude as it is produced in
577 typical auroral fashion by the secondary ions and electrons exciting atmospheric gaseous
578 components. The exponential increase with depth into the atmosphere produces a relatively sharp
579 altitude definition for the lower end of the picket fence posts. The narrow purple band
580 inclination, in contrast, initially follows the path of the remnant meteor material and need not be
581 horizontal.

582 In addition to sputtered secondary ions and electrons that travel down along field lines,
583 another population of upward travelling sputtered particles would travel up along field lines,
584 eventually reaching the opposite hemisphere and producing an array of green picket fence
585 structures of comparable intensity to those seen in the northern hemisphere. In the event that the
586 auroral bombardment ions or electrons have a range greater than the typical size of the remnant
587 dust particles, then the downward flux of secondaries would tend to be greater than the upward
588 flux. On the other hand, for remnant dust particles larger than the range of the bombarding
589 auroral ions, the upward flux would tend to be dominant, as more “backsplash” sputtering would
590 occur. The “strikingly different” upward FAC seen in the STEVE event (Y. Nishimura, 2019)
591 with a conjugate structure in the opposite hemisphere could be associated with the flux of such
592 sputtered secondary “backsplash”. It is possible that the moving lights seen in the ATHA images
593 near 5:41 could be associated with such “backsplash” occurring in a momentarily intense
594 protonic bombardment event acting on the meteor at that time.

595 Among the 1408 ATHA images taken between 5:39 and 7:59 there are a total of 9
596 isolated “flash” events similar to the 5:41 event, but none of them last as long or are as intense. It
597 seems possible that these other isolated flashes are also “backsplash” from sputtering of meteors
598 or sub-visual satellites, but without simultaneous observations of these isolated flashes in other
599 imagers, this is only speculation. It can be seen in the movies included in the supplemental
600 materials that there are very frequent isolated, single frame “flash” events in the LUCK images,

601 but we have not been able to find simultaneous observations of corresponding flashes in any of
602 the other imagers in this case either.

603 Although there are no reports of southern hemisphere streaks for the 2016-7-25 event, it
604 is shown in (Y. Nishimura, 2019) that conjugate streaks are seen in a STEVE event with green
605 picket fence structure, but not in the case of an event without the green picket fence. If the
606 narrow purple streaks seen in STEVE are all produced by ABLES of dust, then they would only
607 be seen in one hemisphere, while secondary sputtered particles of sufficient energy and intensity
608 to produce the green picket fence could produce green picket fence structures seen in both
609 hemispheres.

610 That STEVE events seem to share a common purple hue in photographs can be attributed
611 to the homogeneity of the materials in the dust left in the remnant trails of ionospheric meteors
612 together with the primarily protonic ABLES of these materials.

613 The apparent motion of blobs of luminosity seems to be at a speed of several km/s along
614 the longitudinal extent of STEVE. Rather than an actual motion of the STEVE material, in the
615 present picture, this is an illusory motion that rather corresponds to local peaks of auroral
616 bombarding flux that pass across the remnant dust trail and illuminate different regions of the
617 dust as a function of time. This is just as laser beam directed to different regions of a smoke
618 cloud would appear to produce a moving spot of light, but the motion of this light would not
619 reflect the motion of the smoke particles.

620 6 Novel observations via ABLES

621 ABLES of satellites and meteors provides a good explanation for the variations of their
622 emissions as they pass through regions of concurrent auroral activity. Assuming this explanation
623 is correct, then a much larger number of such events could be detected by correlating images
624 from pairs of cameras as sensitive as the REGI camera by simultaneously observing similar
625 patches of sky during auroral activity from appropriately sited locations. In July 2016, the
626 number of known satellites cataloged in (Kelso, 2019) was 19,751. The number having a perigee
627 less than 2,000 km was 16,506. Among these LEO objects, 14,111 had an orbital inclination
628 angle of $90^{\circ} \pm 30^{\circ}$. On the average, in the 18-minute period during which 31 transient streaks
629 were observed in REGI, approximately 70 of these satellites would have crossed the REGI field
630 of view. It seems that the REGI camera sensitivity was sufficient to detect a substantial fraction
631 of the known satellites that crossed through its field of view.

632 Although the ASI cameras had the virtue of wide spatial coverage, their limited
633 sensitivity greatly reduced the number of events that could be unambiguously identified as high-
634 altitude objects. Future observations of this phenomenon could open a new window for
635 exploration of the ionosphere during periods of auroral activity. The RGB color vignettes shown
636 for the 6 objects in figure 3 illustrates some of the possible additional characterization that could
637 be extracted for these solid bodies.

638 Acknowledgments, Samples, and Data

- 639 • The authors declare no competing interests.
- 640 • The data supporting the conclusions of this work can be readily obtained from the cited
641 references together with the files in the supplemental information
- 642 • The 16-bit registered REGI photographs used in this work are available from
643 <https://doi.org/10.6084/m9.figshare.c.4658714.v1> (Bennett, 2019)

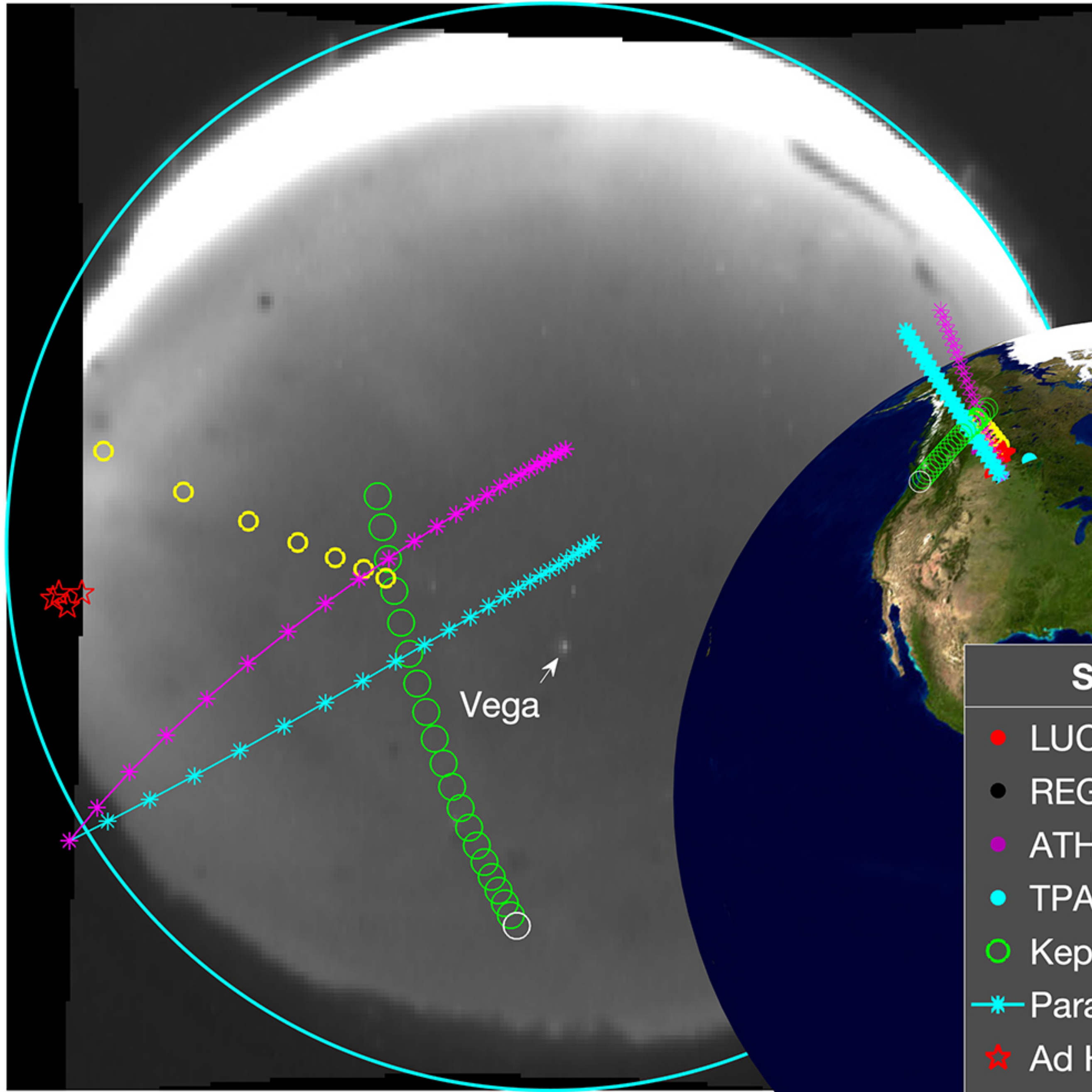
644 **References**

- 645 A. Le Pichon, J. G. (2002). Trail in the atmosphere of the 29 December 2000 meteor as recorded in Tahiti:
646 Characteristics and trajectory reconstitution. *Journal of Geophysical Research*, 107(D23), 4709-4718.
- 647 A. Olech, P. Z. (2013). PF191012 Myszyniec-highest Orionid meteor ever recorded. *Astronomy & Astrophysics*.
- 648 B. Gallardo-Lacourt, J. L. (2018). On the Origin of STEVE: Particle Precipitation or Ionospheric Skyglow?
649 *Geophysical Research Letters*, 1-6.
- 650 B. Gallardod-Lacourt, Y. N. (2018). A Statistical Analysis of STEVE. *Journal of Geophysical Research: Space*
651 *Physics*, 9893-9905.
- 652 B.J. Jackel, C. U. (2014). Auroral spectral estimation with wide-band color mosaic CCDs. *Geoscientific*
653 *Instrumentation Methods and Data Systems*, 3, 71-94.
- 654 Bennett, C. (2019, September). *Collection of Images for Journal of Geophysical Research Article "Auroral*
655 *Illumination of Solid Bodies"*. Retrieved from figshare: <https://doi.org/10.6084/m9.figshare.c.4658714.v1>
- 656 Bettonvil, F. (2005). Imaging Fisheye Lenses. *WGN, Journal of the International Meteor Organization*, 33(1), 9-
657 14.
- 658 CIRES. (2019, July). *POMME-10 MAGNETIC MODEL OF THE EARTH*. Retrieved from
659 <http://geomag.colorado.edu/pomme-10-magnetic-model-of-the-earth.html>
- 660 D. Lummerzheim, M. G. (2001). Emission of OI(630 nm) in proton aurora. *Journal of Geophysical Research*, 141-
661 148.
- 662 D.M. Gillies, E. D.-L. (2019). First Observations From the TREx Spectrograph: The Optical Spectrum of STEVE
663 and the Picket Fence Phenomena. *Geophysical Research Letters*, 7207-7213.
- 664 E. A. MacDonald, E. D.-L. (2018). New science in plain sight: Citizen scientists lead to the discovery of optical
665 structure in the upper atmosphere. *Science Advances*, 1-5.
- 666 E. Mishin, Y. N. (2017). SAPS/SAID revisited: A causal relation to the substorm current wedge. *Journal of*
667 *Geophysical Research: Space Physics*, 8516-8535.
- 668 G. Liu, S. E. (2013). Comparison of drift velocities of nighttime equatorial plasma depletions with ambient plasma
669 drifts and thermospheric neutral winds. *Journal of Geophysical Research: Space Physics*, 7360-7368.
- 670 Hoffleit, D. a. (2014, January). *Yale Bright Star Catalog*. Retrieved from [http://tdc-](http://tdc-www.harvard.edu/catalogs/bsc5.html)
671 [www.harvard.edu/catalogs/bsc5.html](http://tdc-www.harvard.edu/catalogs/bsc5.html)
- 672 Johnstone, A. (1978). Pulsating aurora. *Nature*, 274, 119-126.
- 673 Jun Liang, E. D. (2016). On the 630 nm red-line pulsating aurora: Red-line Emission Geospace Observaotry
674 observations and model simulations. *Journal of Geophysical Research: Space Physics*, 121, 7988-8012.
- 675 K.A. Hill, L. R. (2004). Sputtering and High Altitude Meteors. *Earth, Moon, and Planets*, 95, 403-412.
- 676 Kelso, T. (2019, 8). *CelesTrak Home Page*. Retrieved from [Celestrak.com](https://celestrak.com)
- 677 Levin, B. Y. (1963). Fragmentation of Meteoric Bodies. *Soviet Astronomy*, 233-238.
- 678 Mathworks. (2019, July). *Mathworks*. Retrieved from [mathworks.com](https://www.mathworks.com)
- 679 P. Lognonne, e. a. (2006). Seismic waves in the ionosphere. *Europhysics news*, 37(4), 11-14.
- 680 Plane, J. M. (2012). Cosmic dust in the earth's atmosphere. *Chemical Society Review*, 41, 6507-6518.
- 681 S.B. Mende, M. T. (2019). Color Ratios of Subauroral (STEVE) Arcs. *Journal of Geophysical Research: Space*
682 *Physics*.
- 683 Solomon, S. C. (2001). Auroral particle transport using Monte Carlo and hybrid methods. *Journa of Geophysical*
684 *Research*, 106, 107-116.
- 685 Thomas, G. (1979). Bombardment-Induced Light Emission. *Surface Science*, 381-416.
- 686 Townsend, P. C. (2005). Sputtering by electrons and photons. In e. R. Behrish, *Sputtering by Particle Bombardment*
687 *II* (Vol. 52, pp. 147-178). Springer-Verlag.
- 688 University of Calgary. (2018, 12 9). *UofC Space Physics Data Portal*. Retrieved from [https://data-](https://data-portal.phys.ucalgary.ca)
689 [portal.phys.ucalgary.ca](https://data-portal.phys.ucalgary.ca)
- 690 Vinkovic, D. (2007). Thermalization of sputtered particles as the source of diffuse radiation from high altitude
691 meteors. *Advances in Space Research*, 39, 574-582.
- 692 W.E. Archer, B. G.-L.-M. (2019). Steve: The Optical Signature of Intense Subauroral Ion Drifts. *Geophysical*
693 *Research Letters*, 6279-6286.
- 694 Weisstein, E. (2109, July 22). *Gnomonic Projection*. Retrieved from
695 <http://mathworld.wolfram.com/GnomonicProjection.html>
- 696 X. Chu, D. M.-L. (2019). Identifying the magnetospheric driver of STEVE. *Geophysical Research Letters*.
- 697 Y. Fujiwara, M. U. (1998, February 1). Meteor luminosity at 160 km altitude from TV observations for bright
698 Leonid meteors. *Geophysical Research Letters*, 25(3), 285-288.

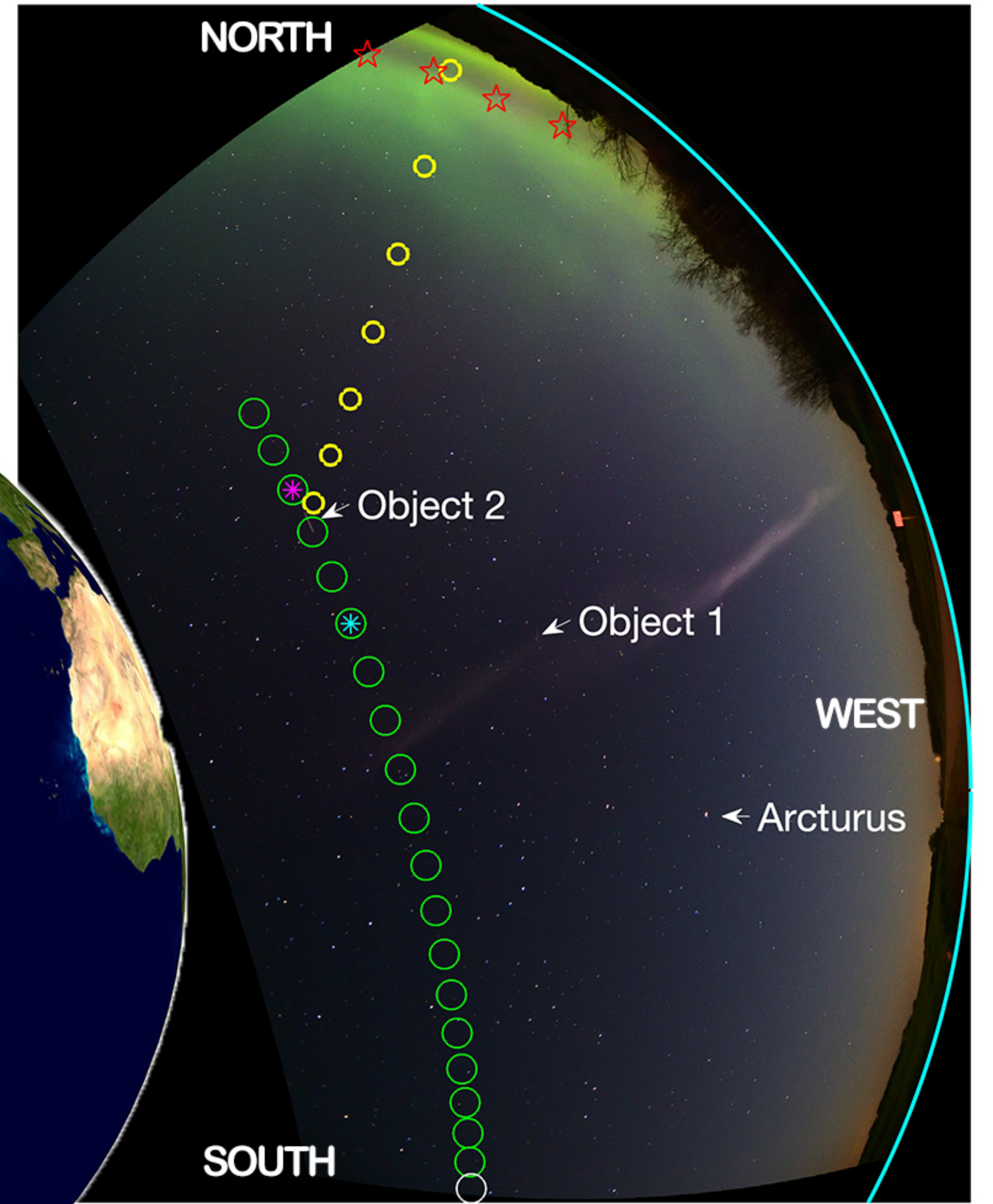
- 699 Y. Nishimura, B. G.-L. (2019). Magnetospheric Signatures of STEVE: Implications for the Magnetospheric Energy
700 Source and Interhemispheric Conjugation. *Geophysical Research Letters*, 5637-5644.
701 Yamamoto, T. (1988, February 1). On the temporal fluctuations of pulsating auroral luminosity. *Journal of*
702 *Geophysical Research*, 93(A2), 897-911.
703

Figure 1.

ATHA 05:54:47

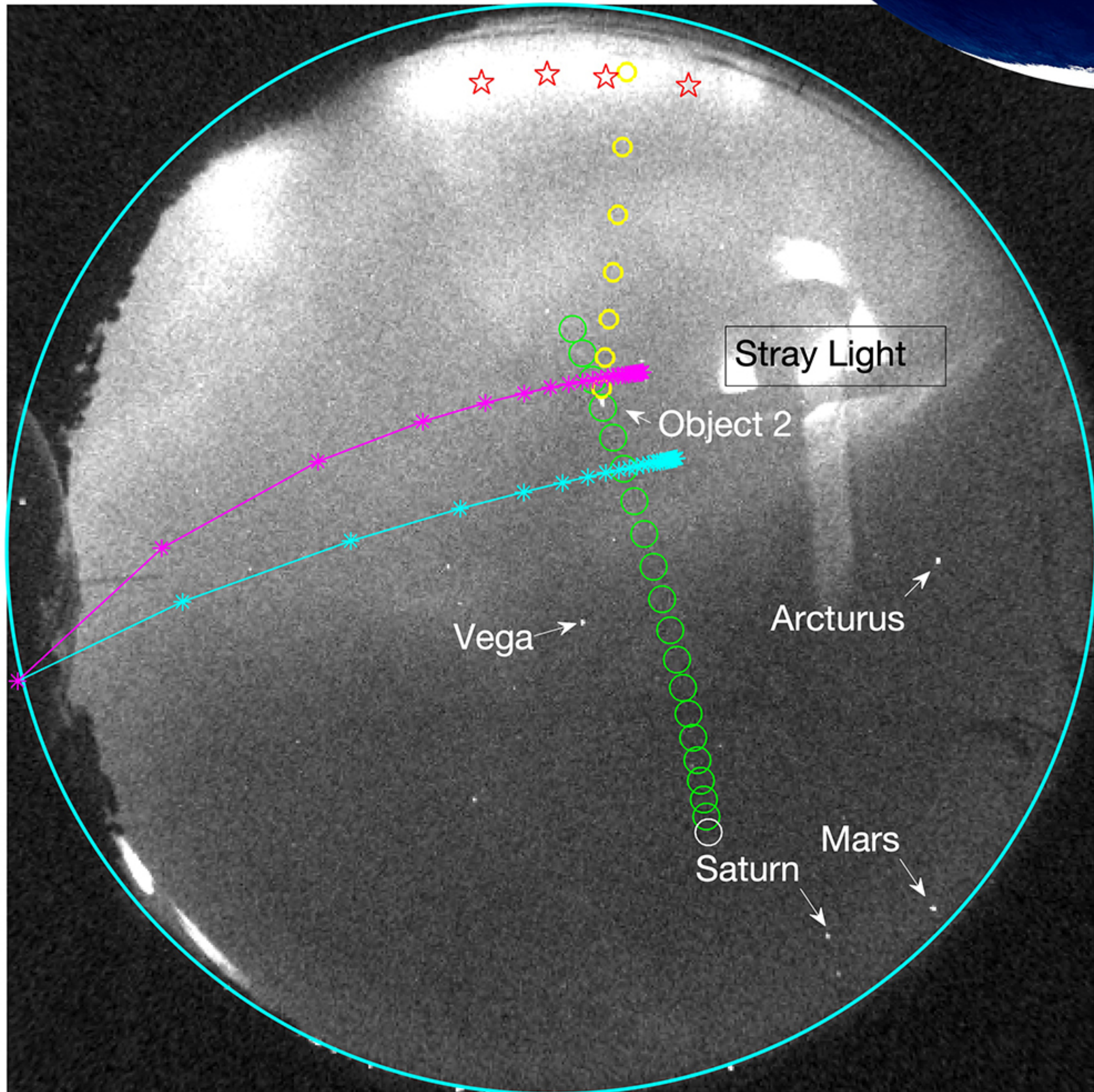


REGI 05:54:48



Symbol Key	
●	LUCK Gnd Station
●	REGI Gnd Station
●	ATHA Gnd Station
●	TPAS Gnd Station
○	Keplerian Trajectory
*	Parallax Tracks
★	Ad Hoc Points
○	Magnetic Field Points

LUCK 05:54:47



REGI 05:54:48

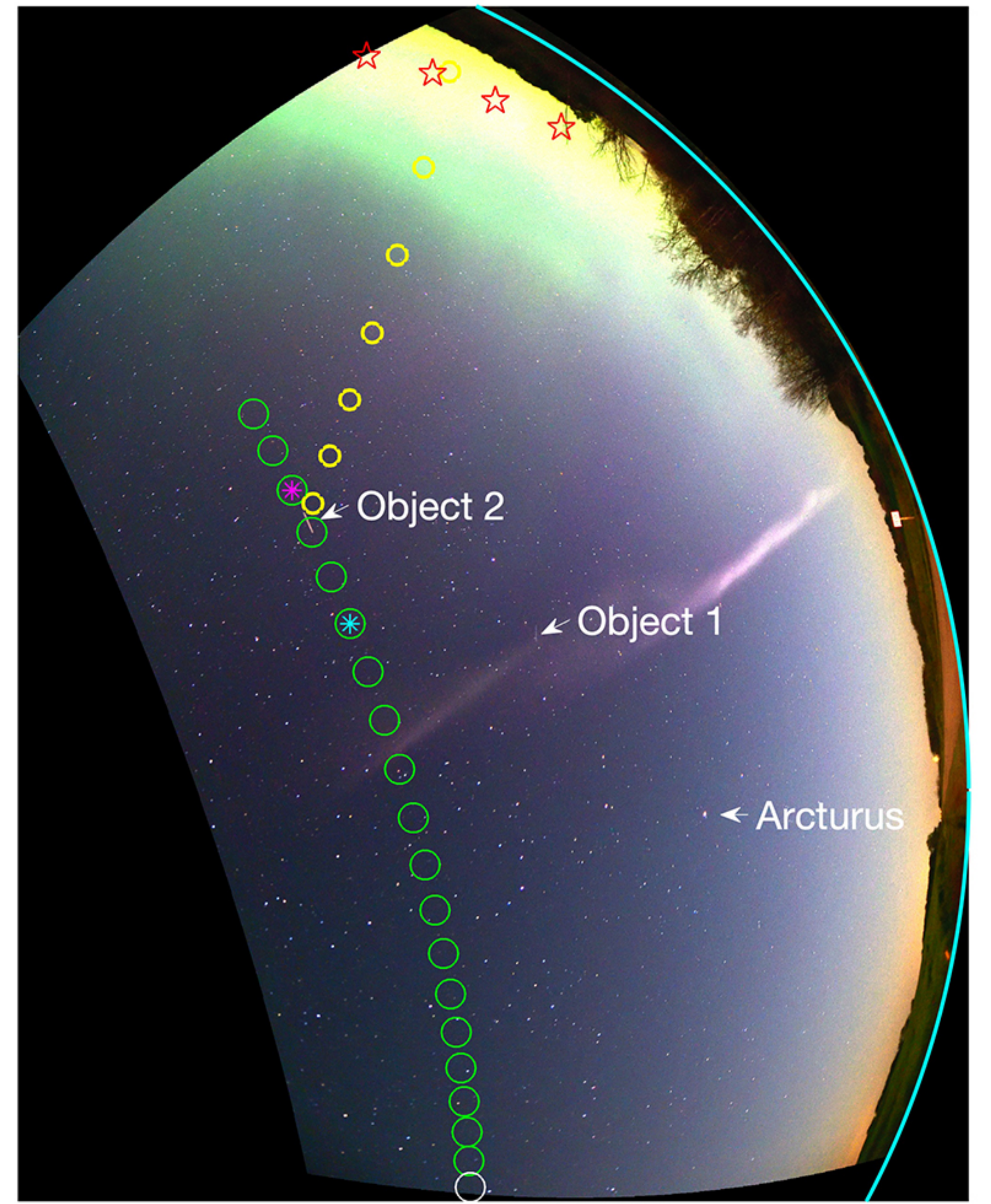
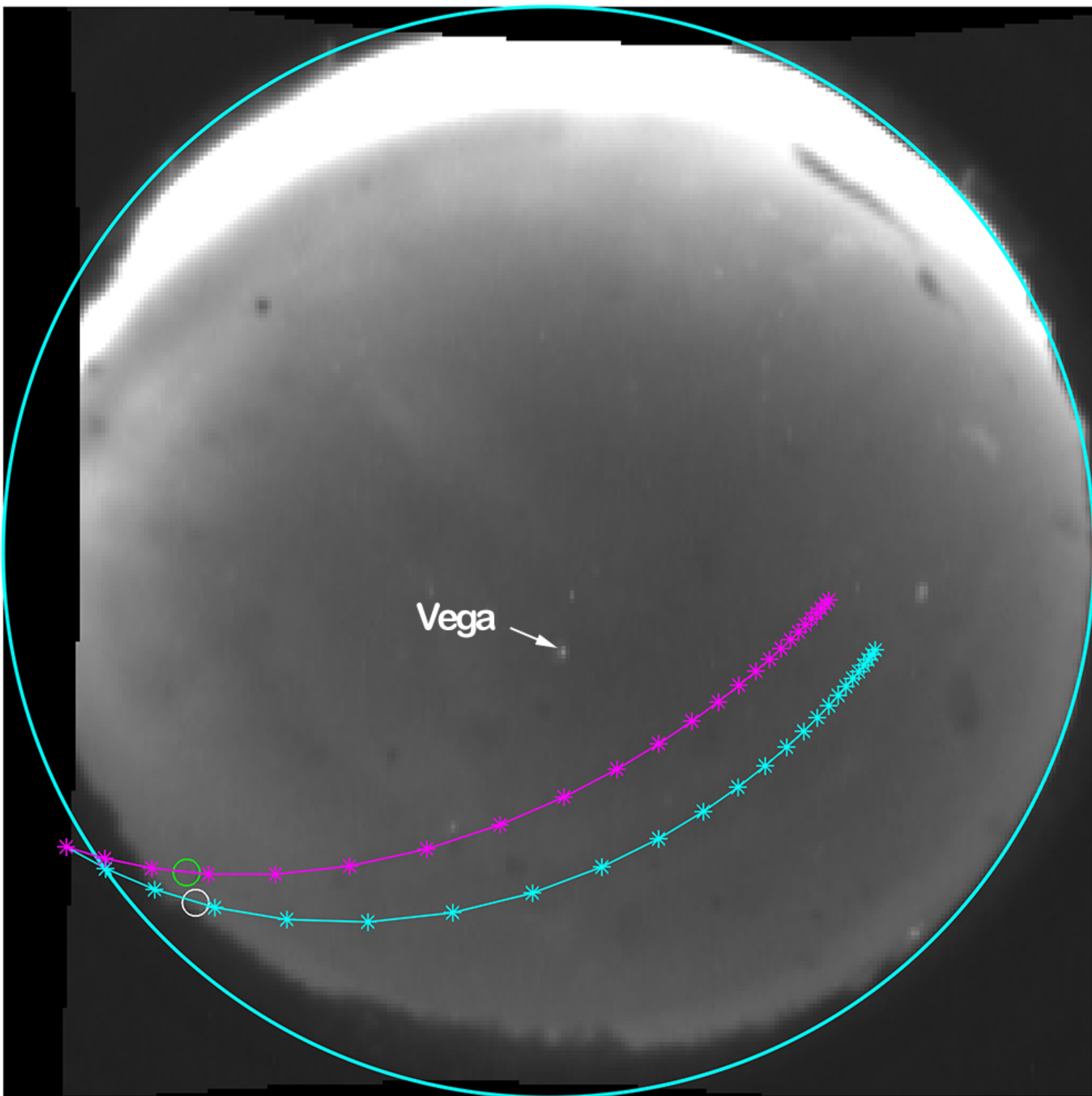
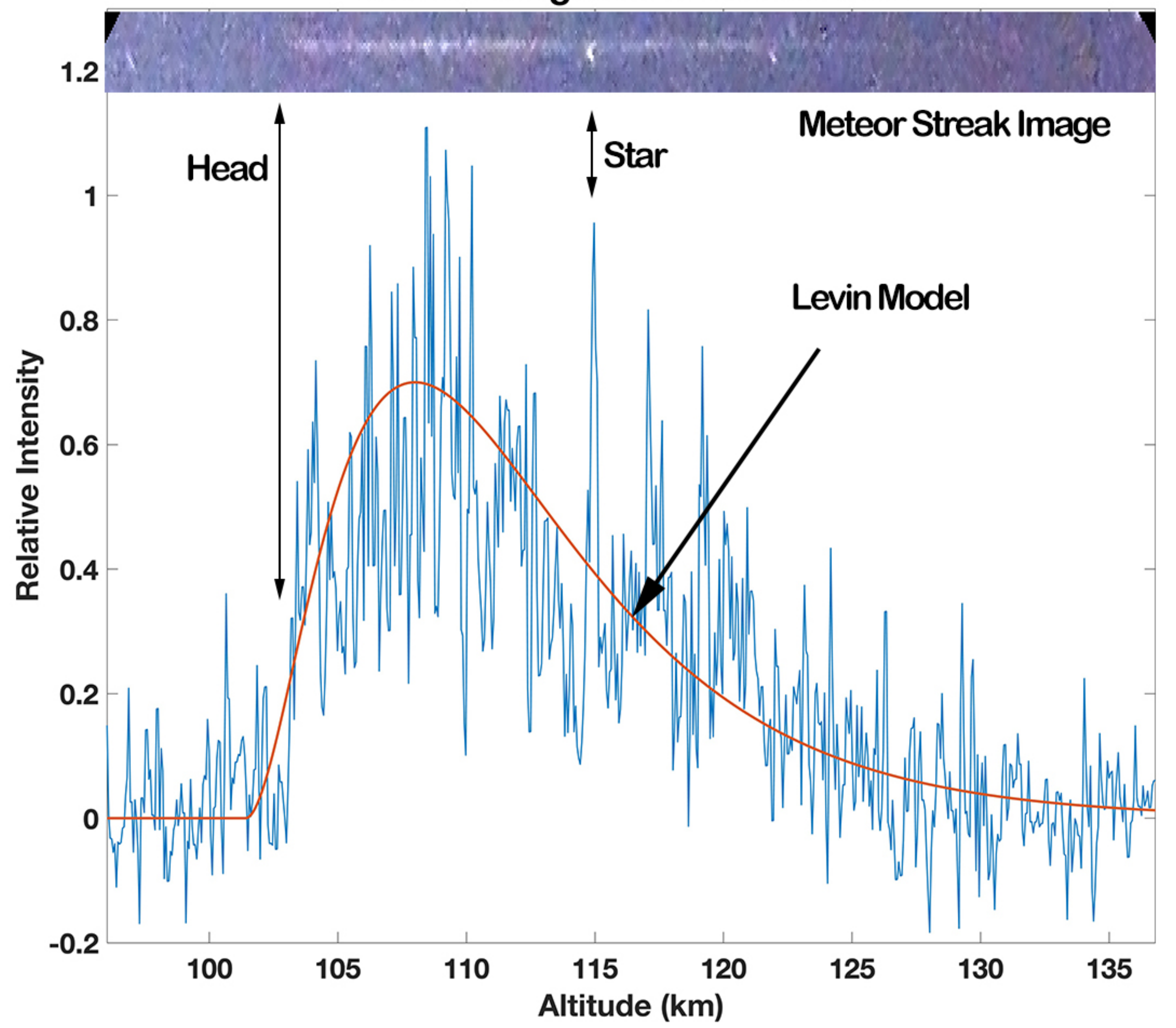


Figure 2.

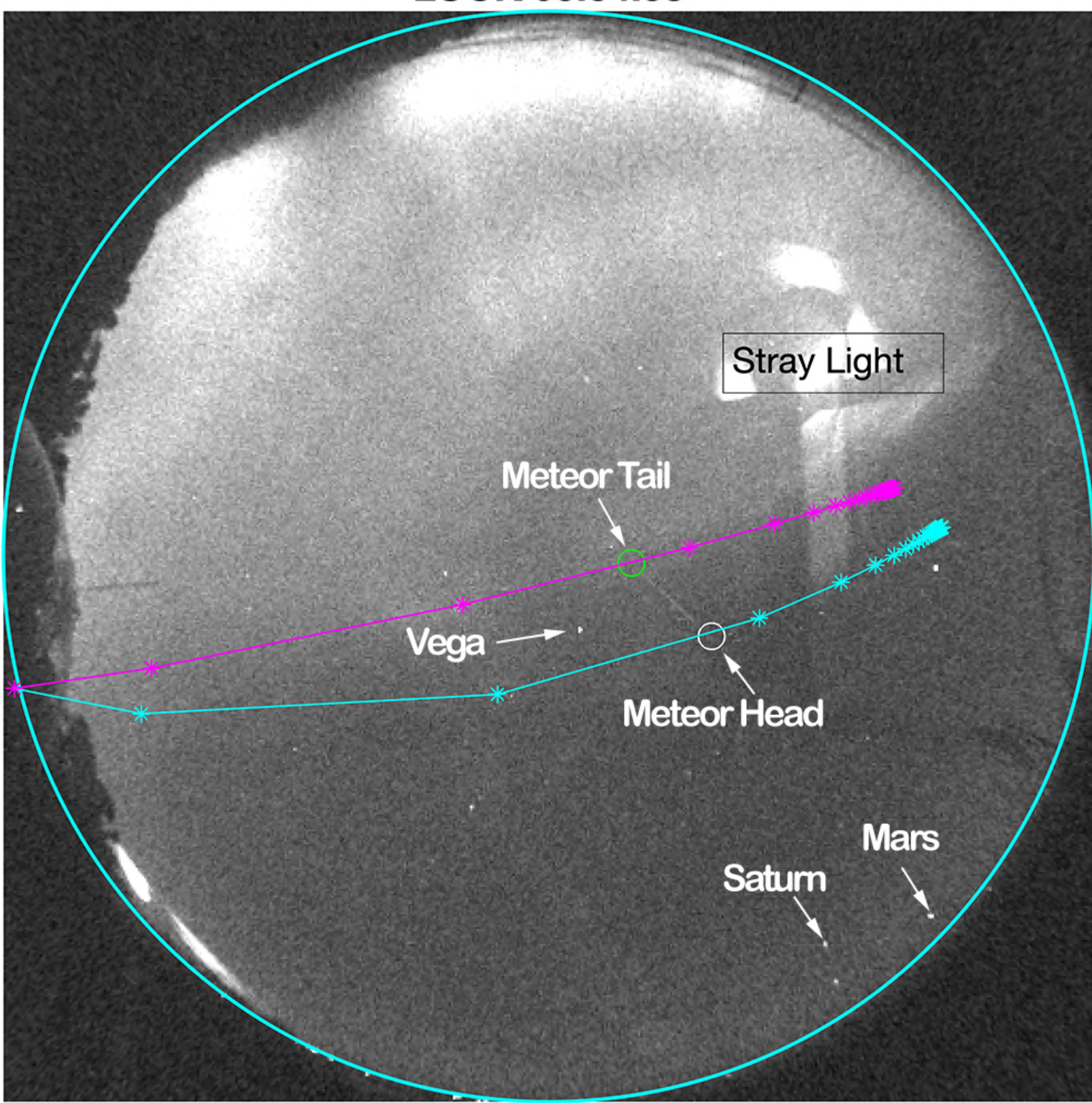
ATHA 05:54:35



Meteor Brightness vs. Altitude



LUCK 05:54:38



REGI 05:54:39

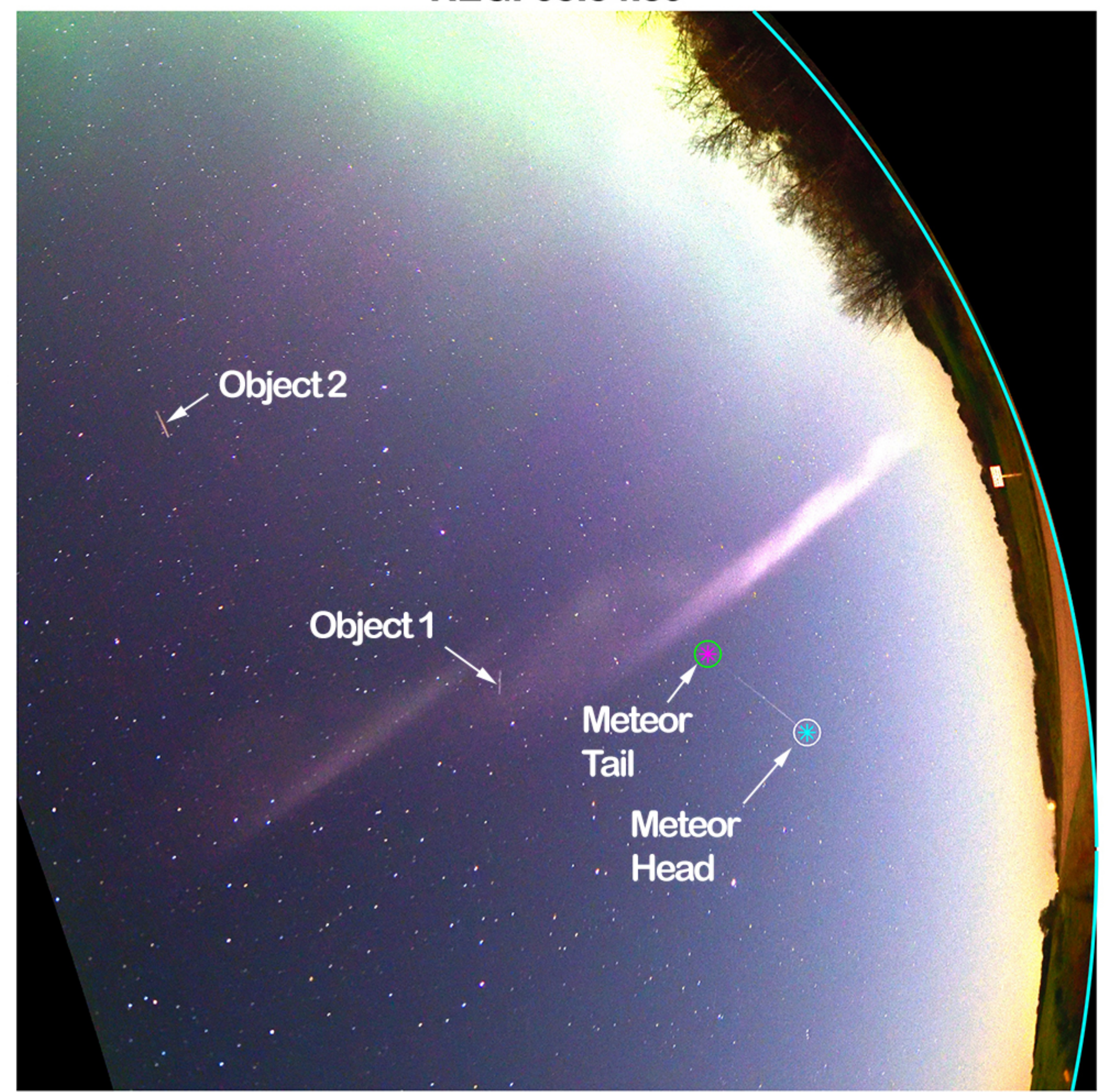


Figure 3.

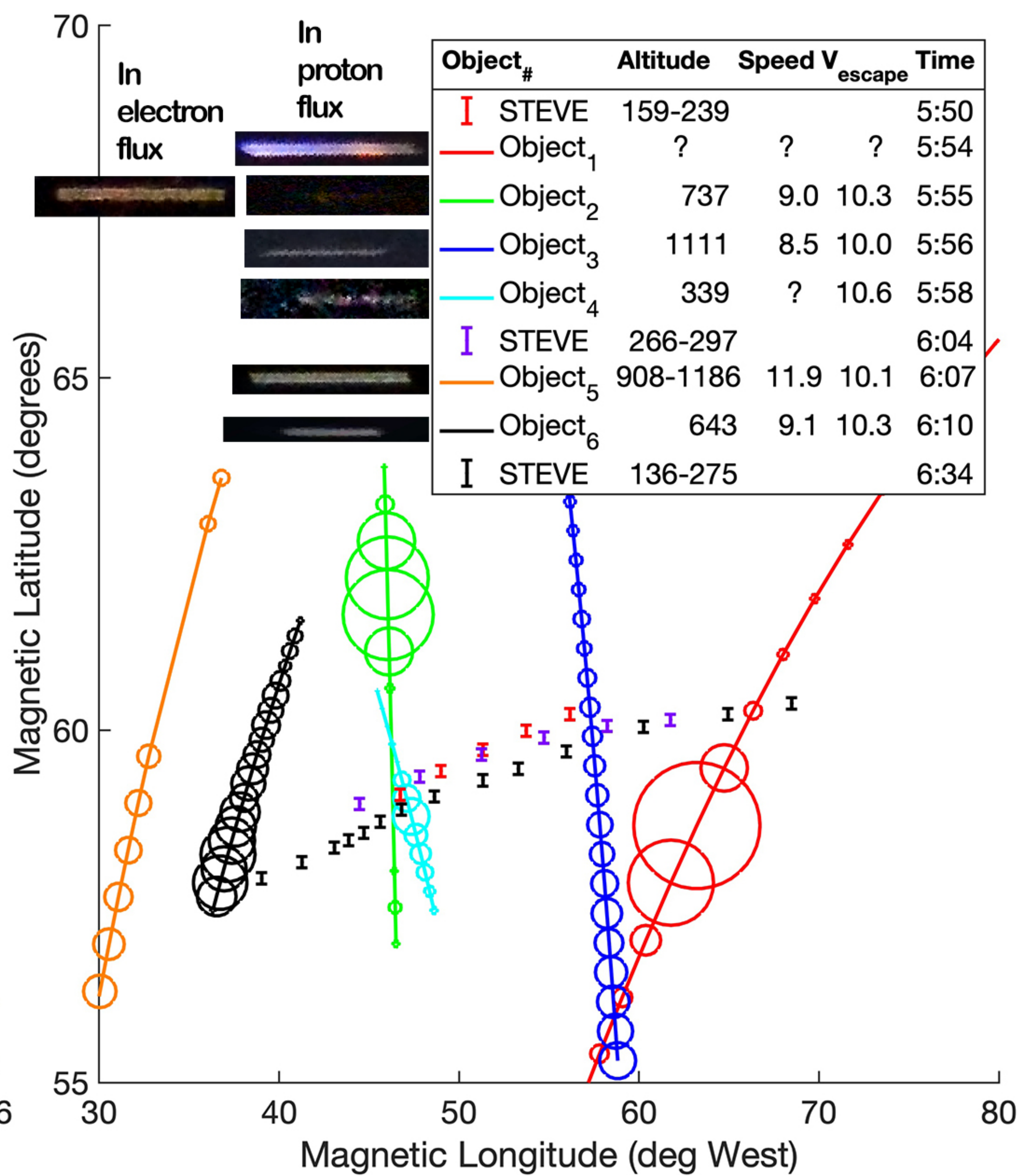
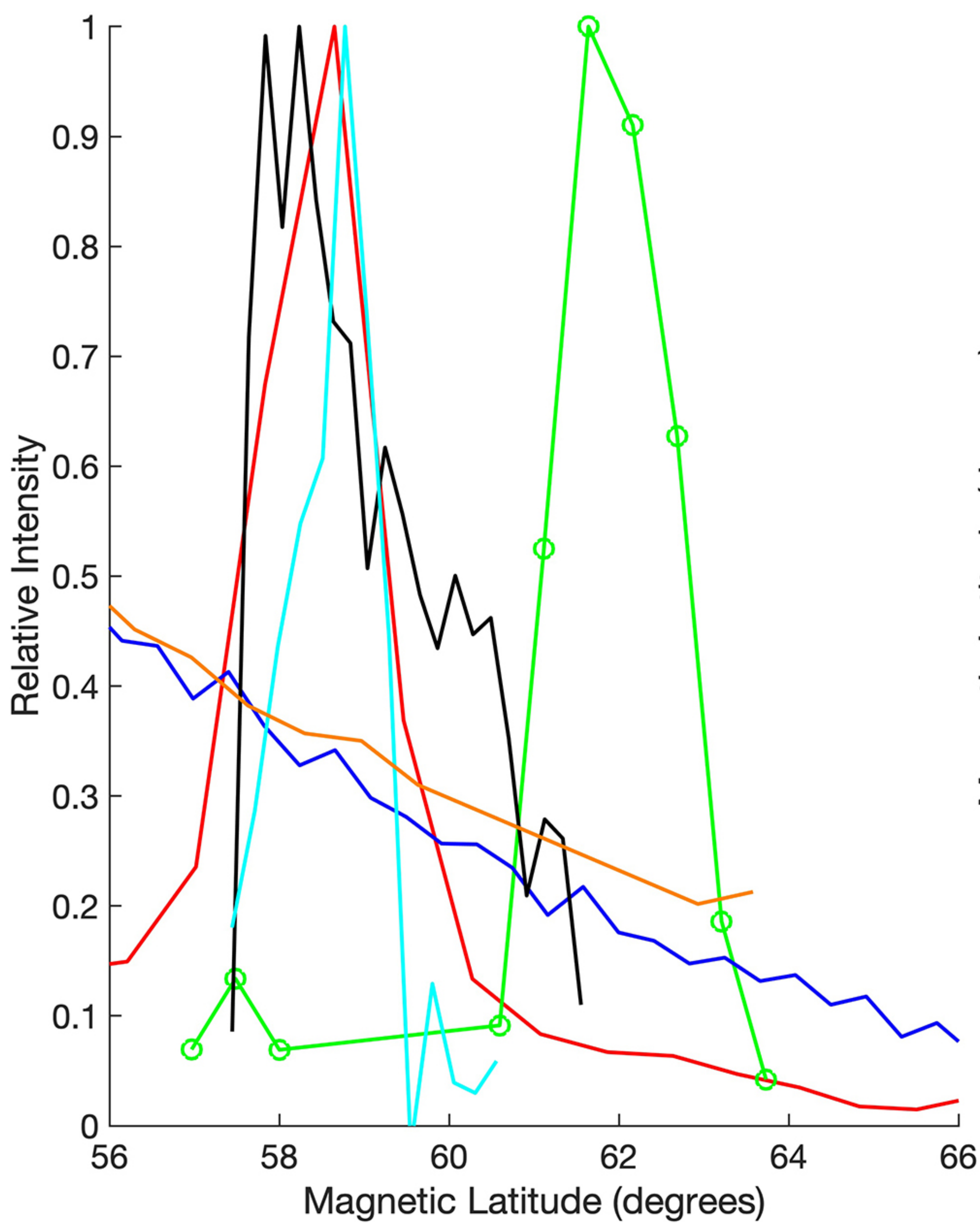
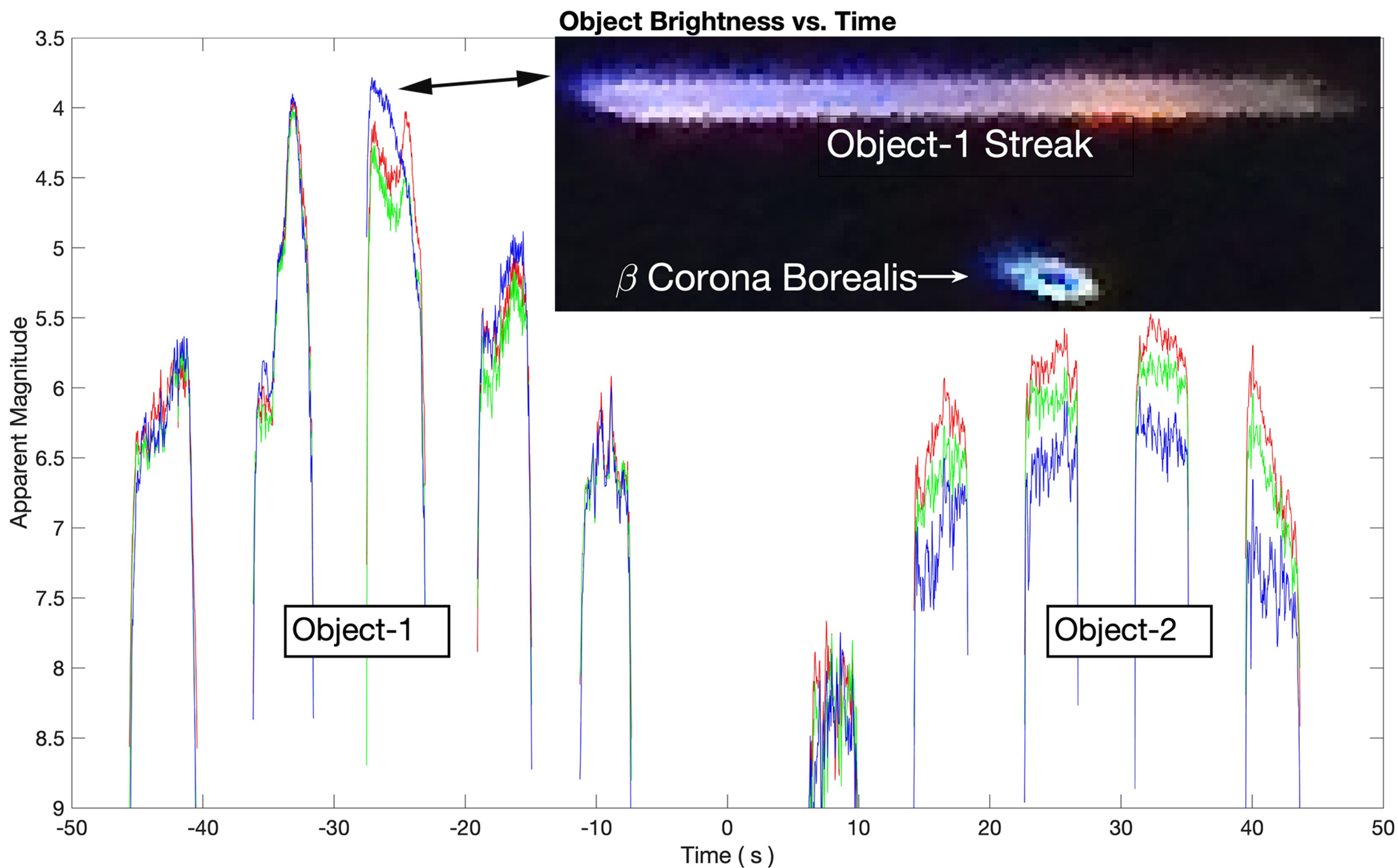


Figure 4.

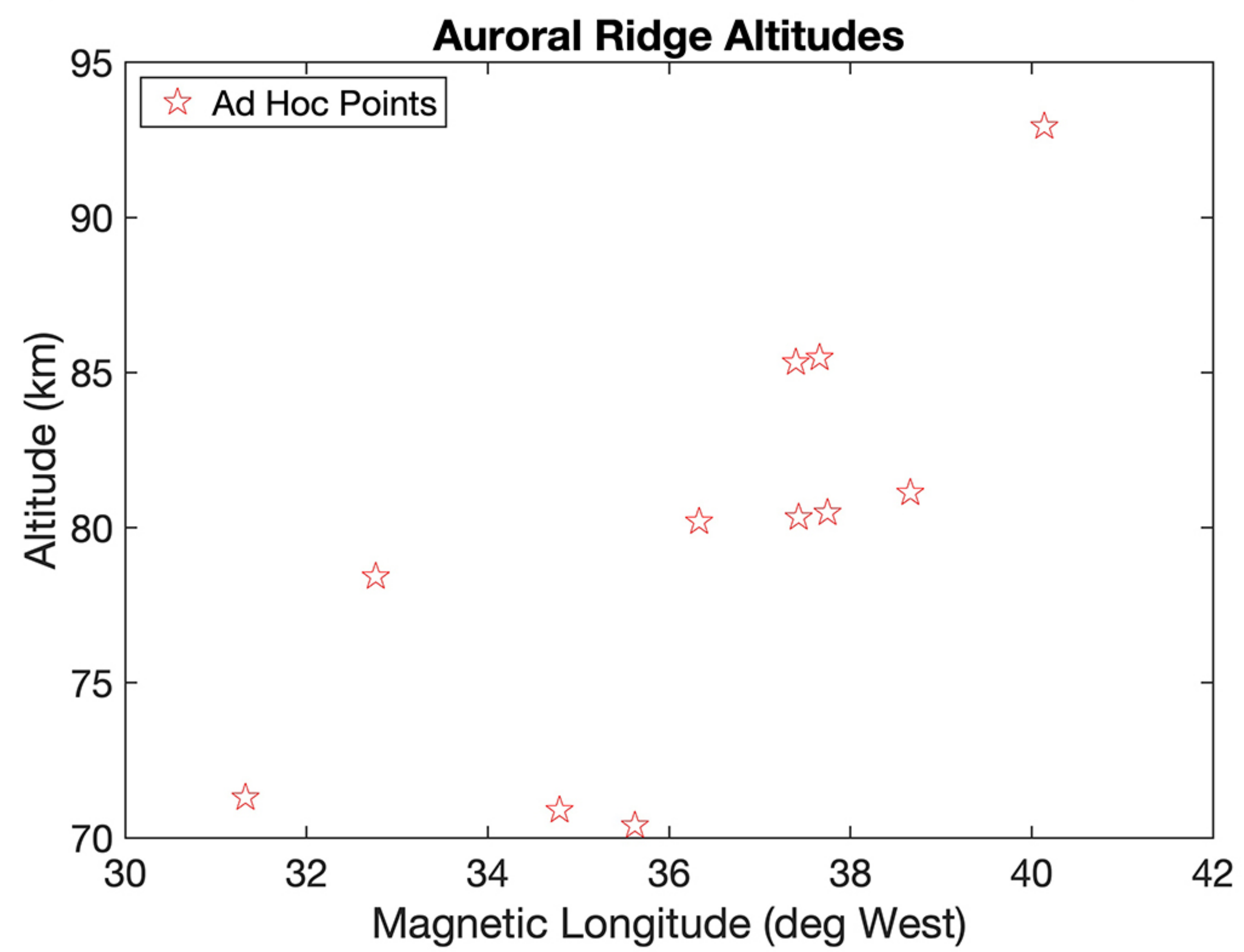
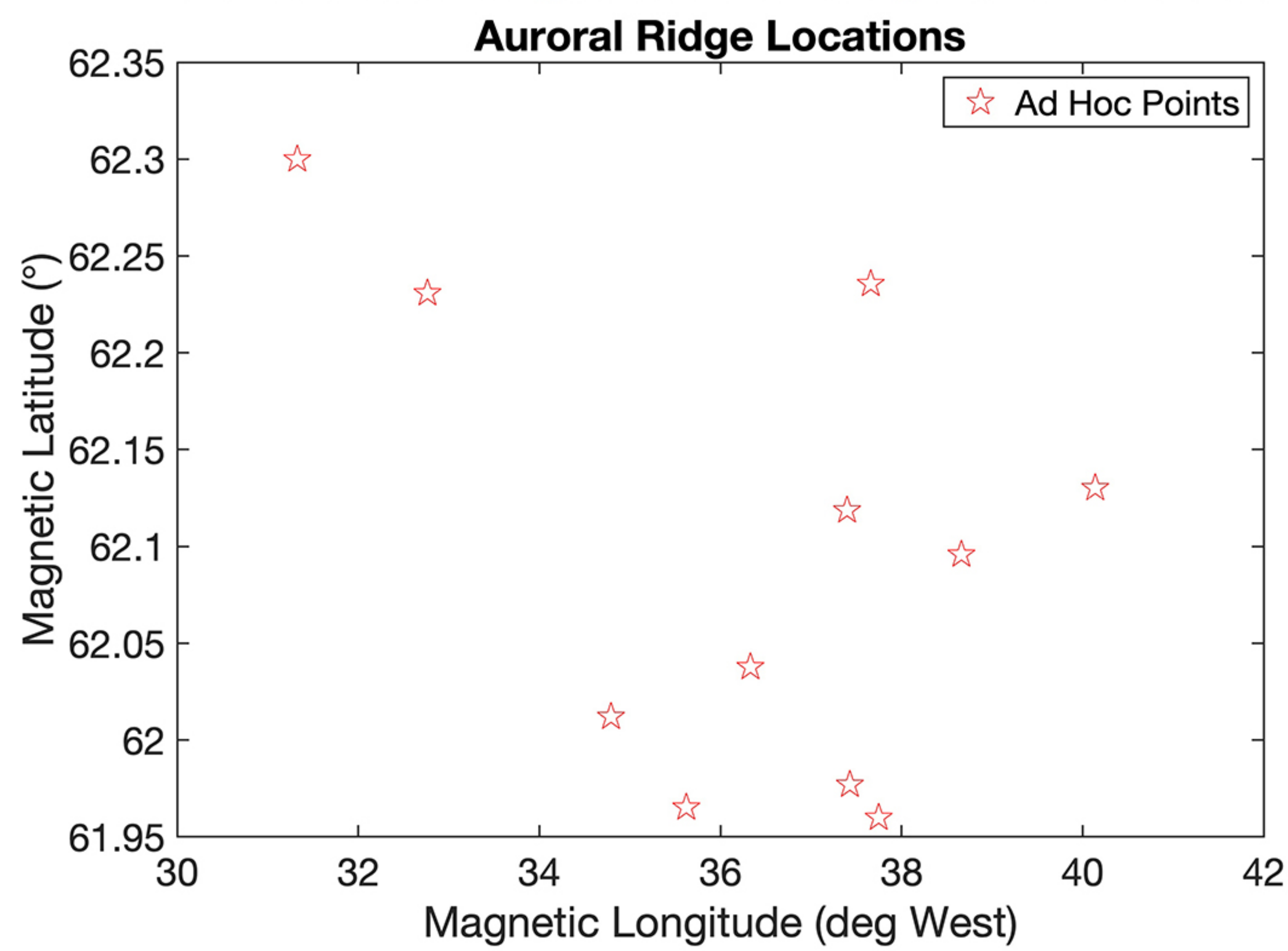
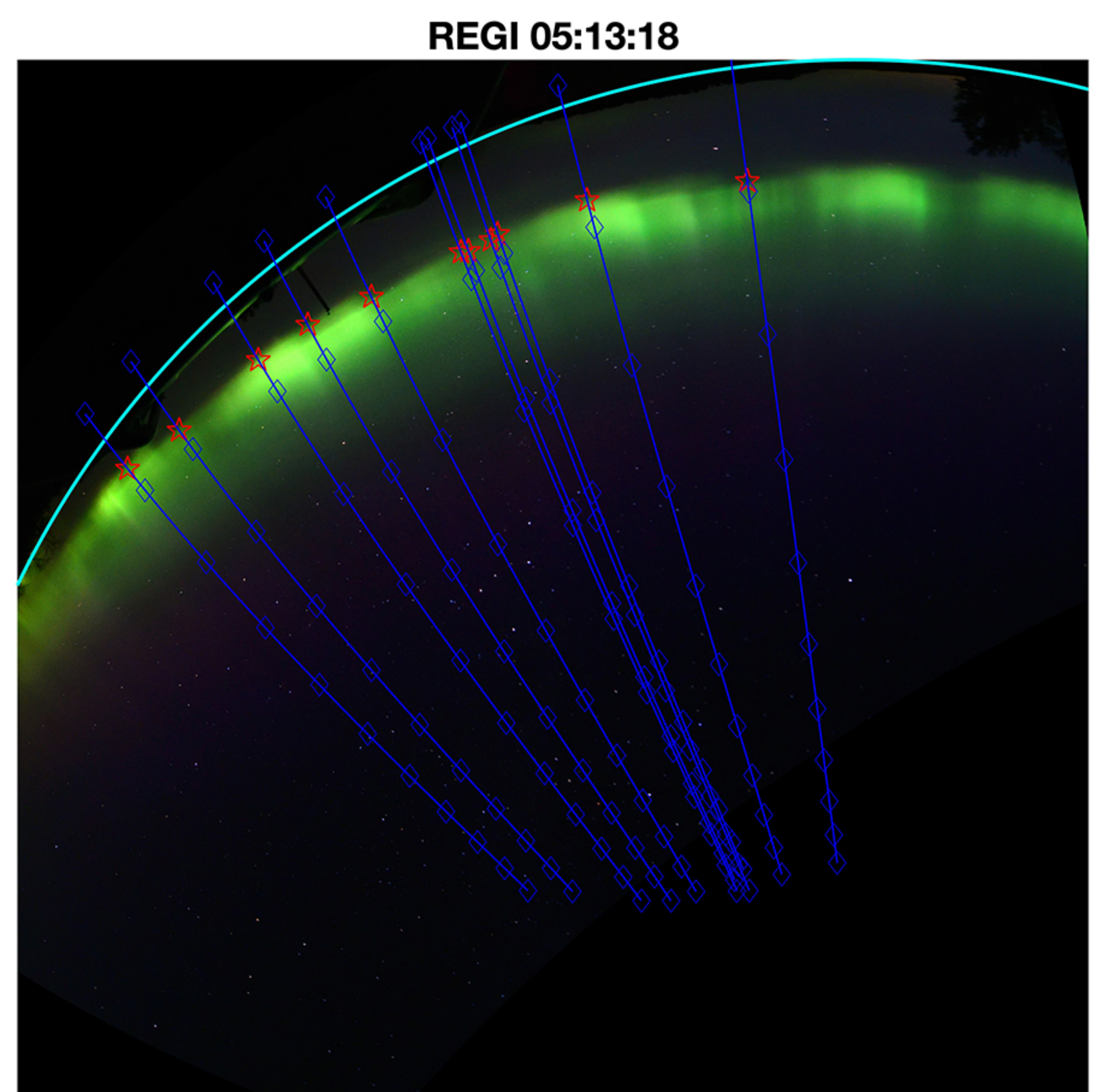
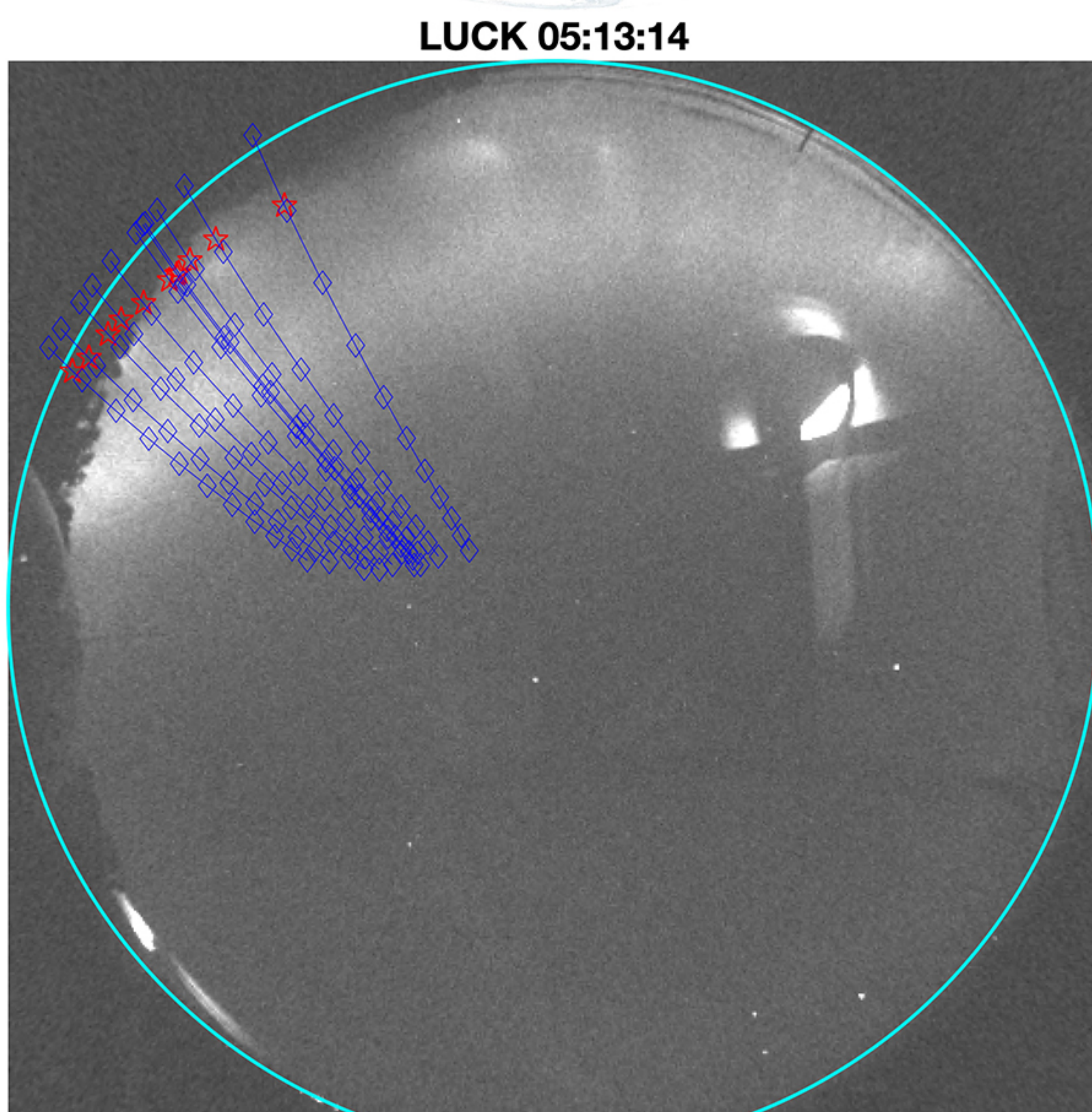
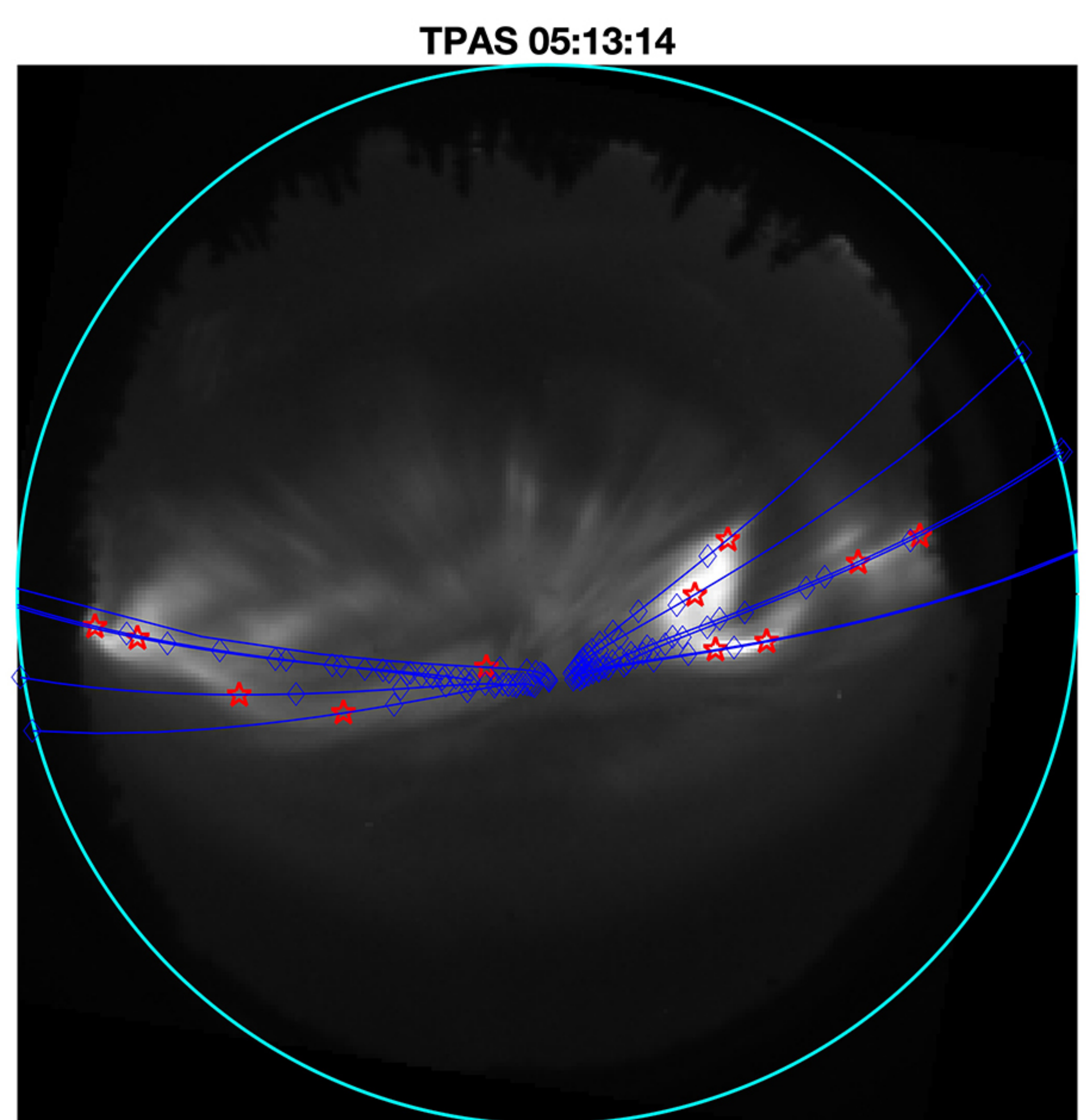
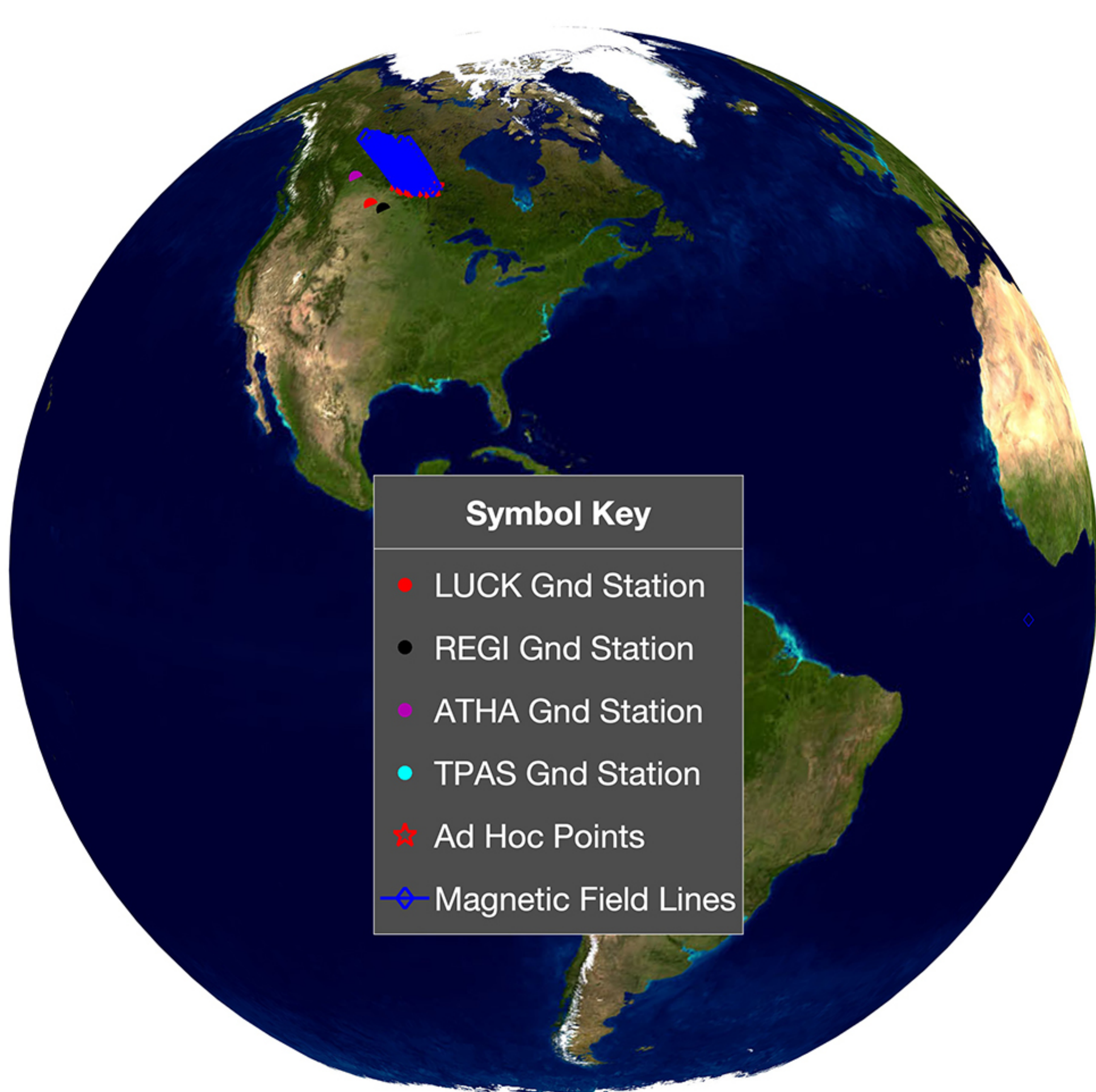
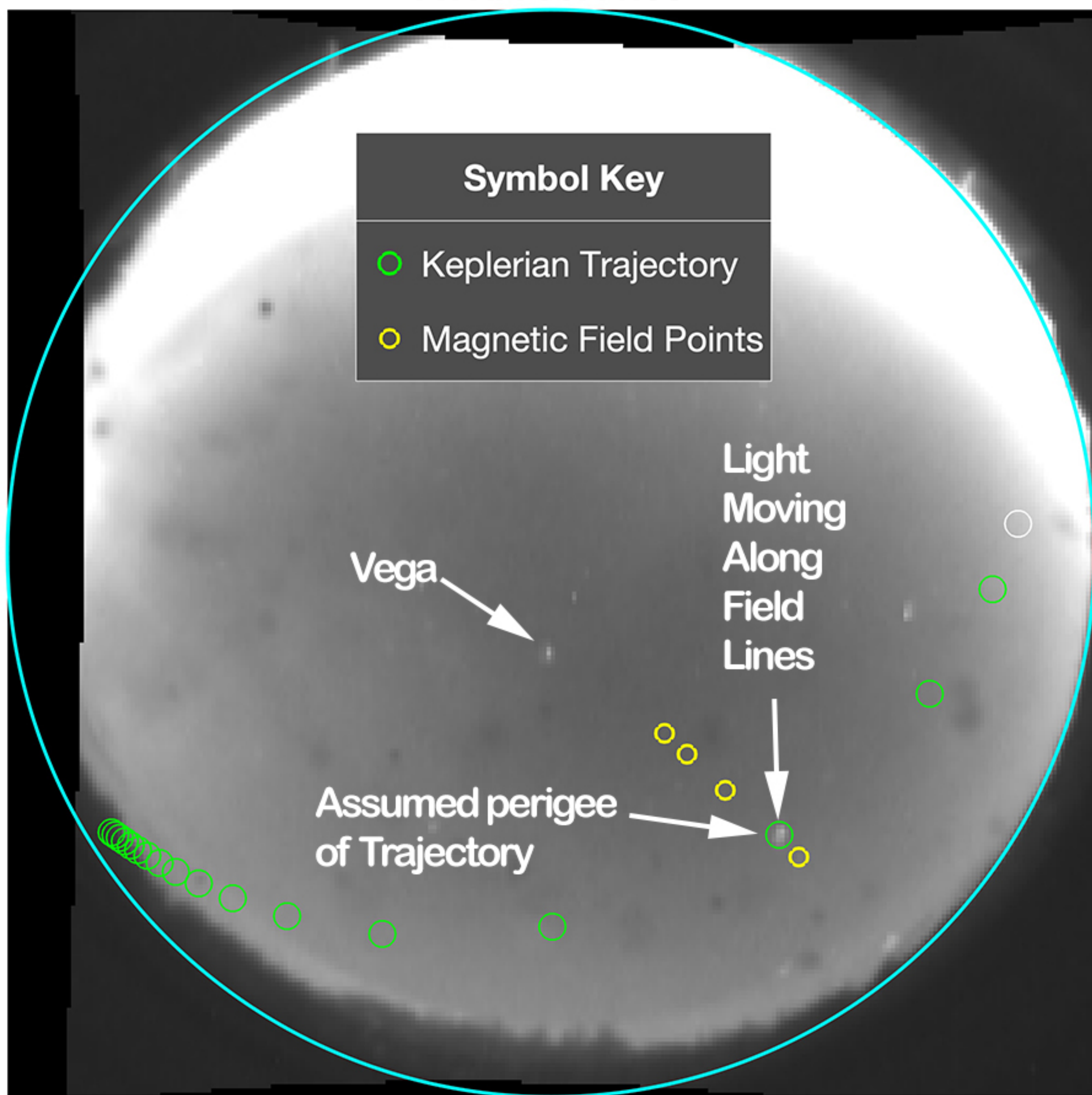
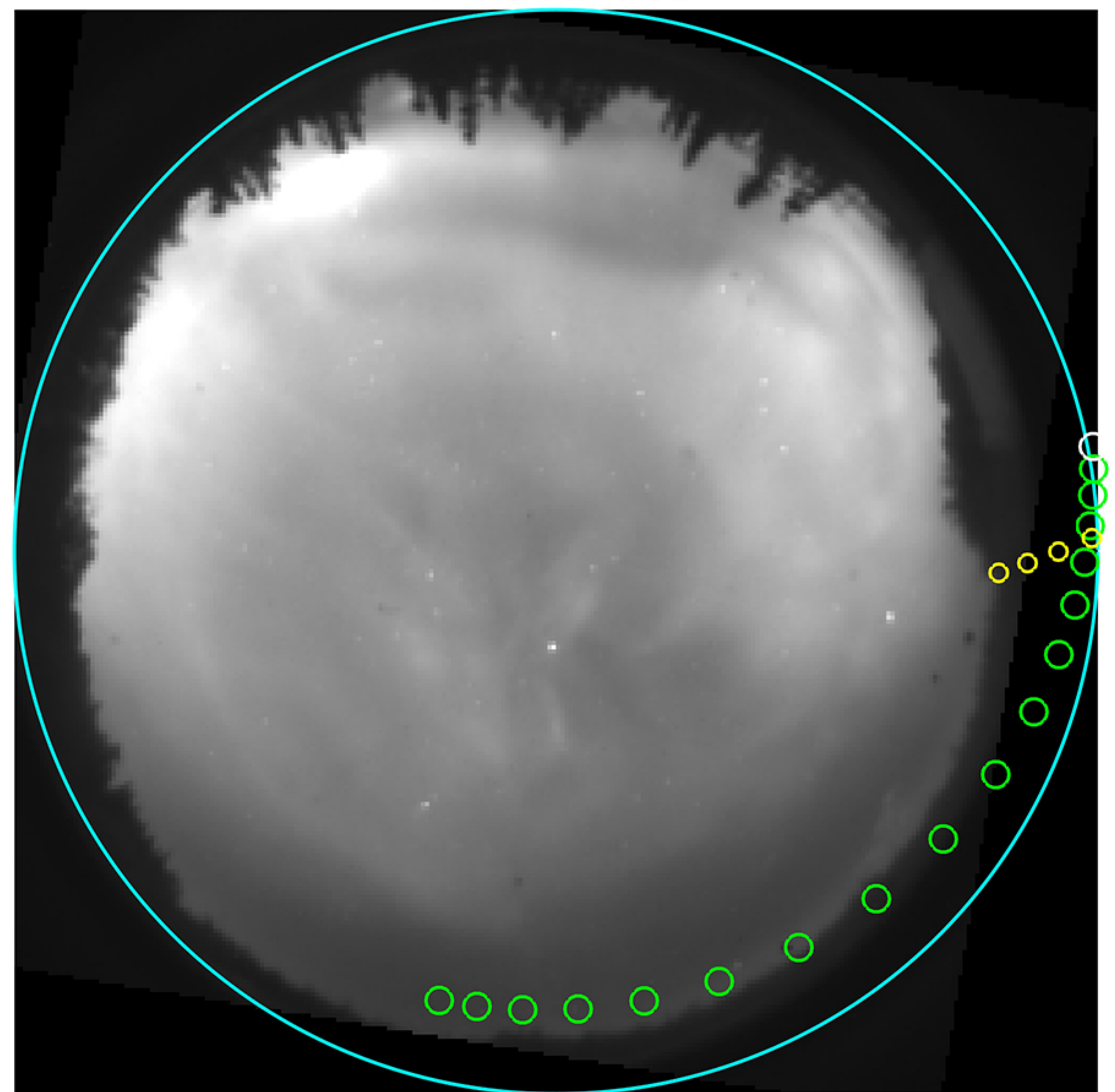


Figure 5.

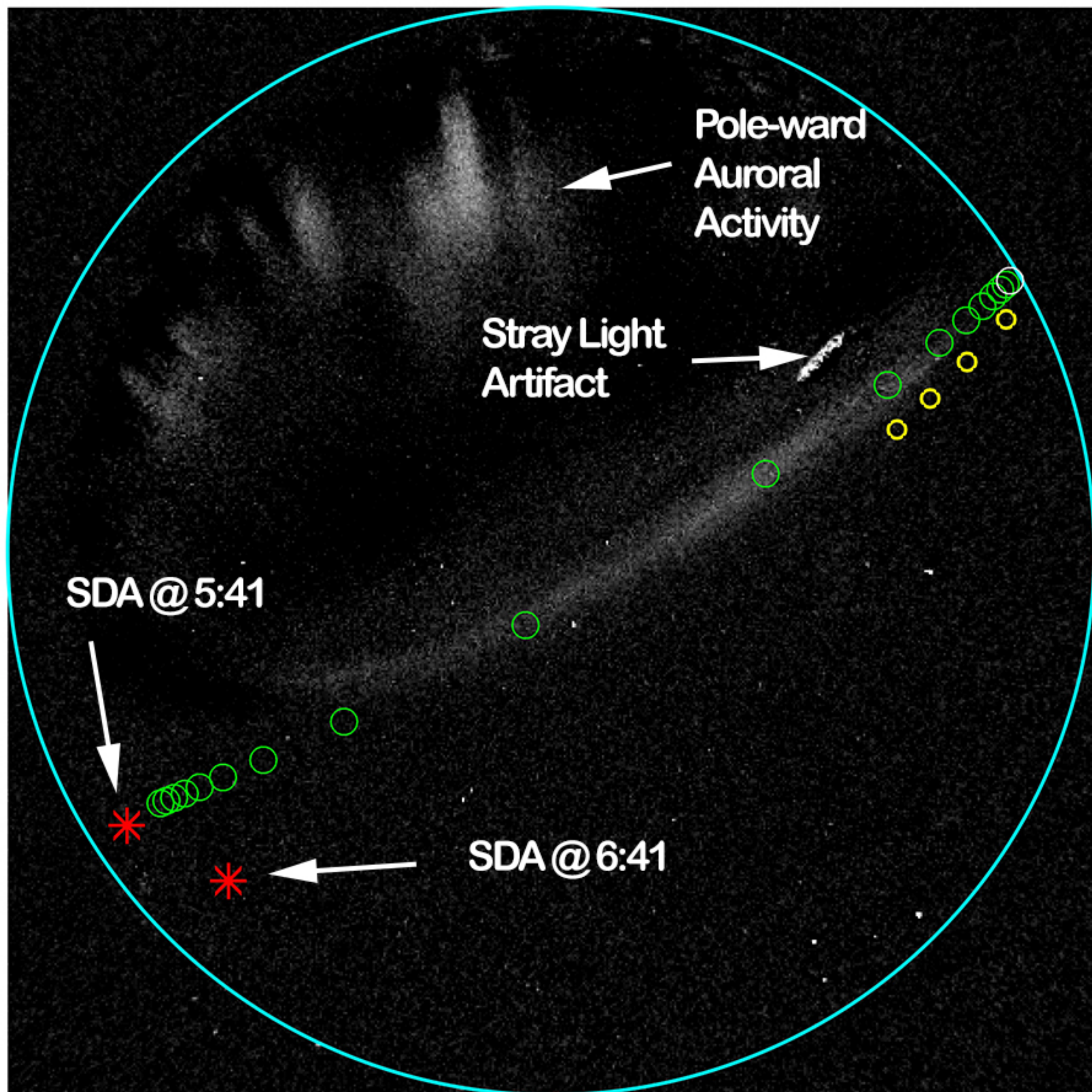
ATHA 05:41:05



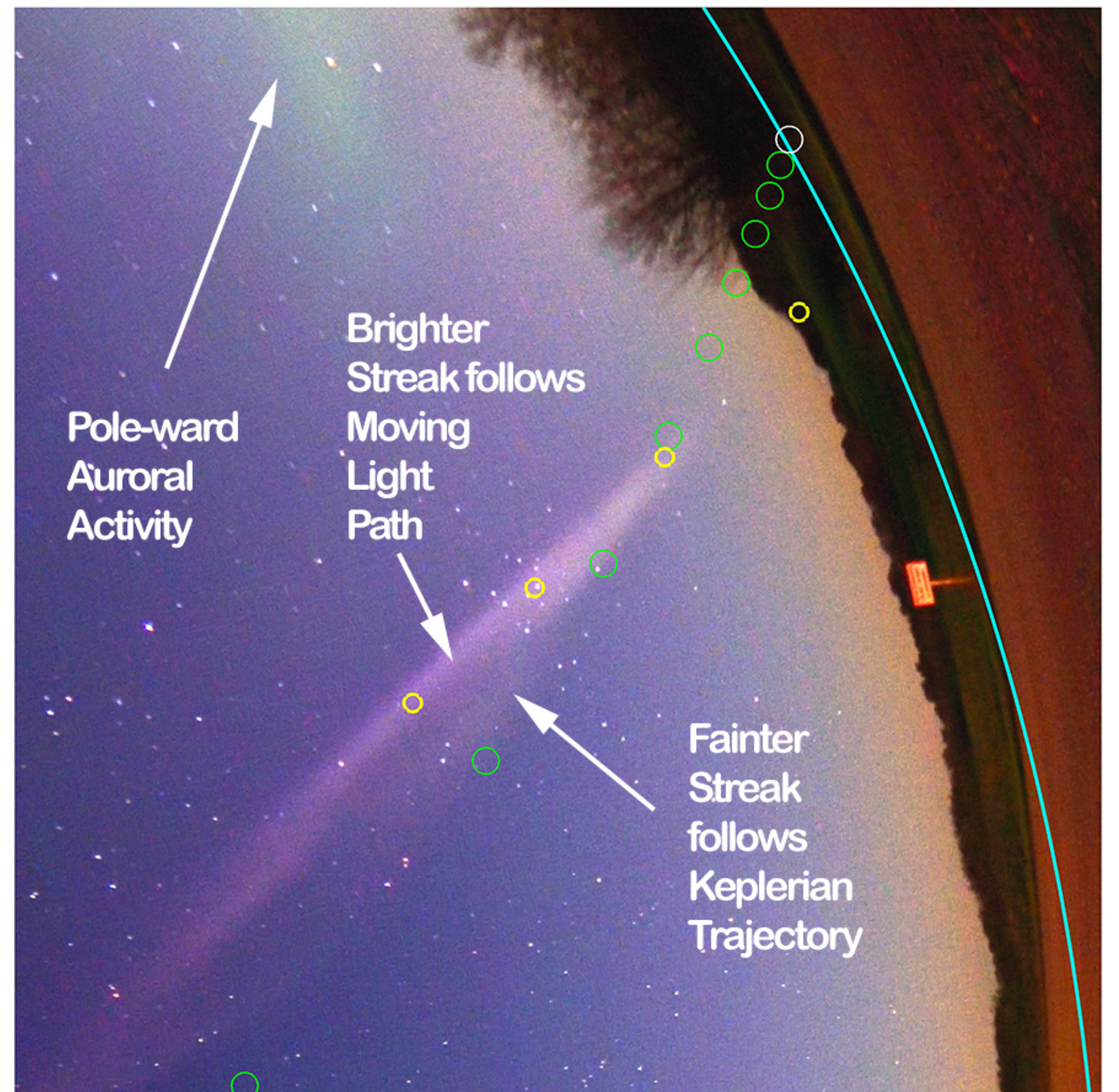
TPAS 05:46:32



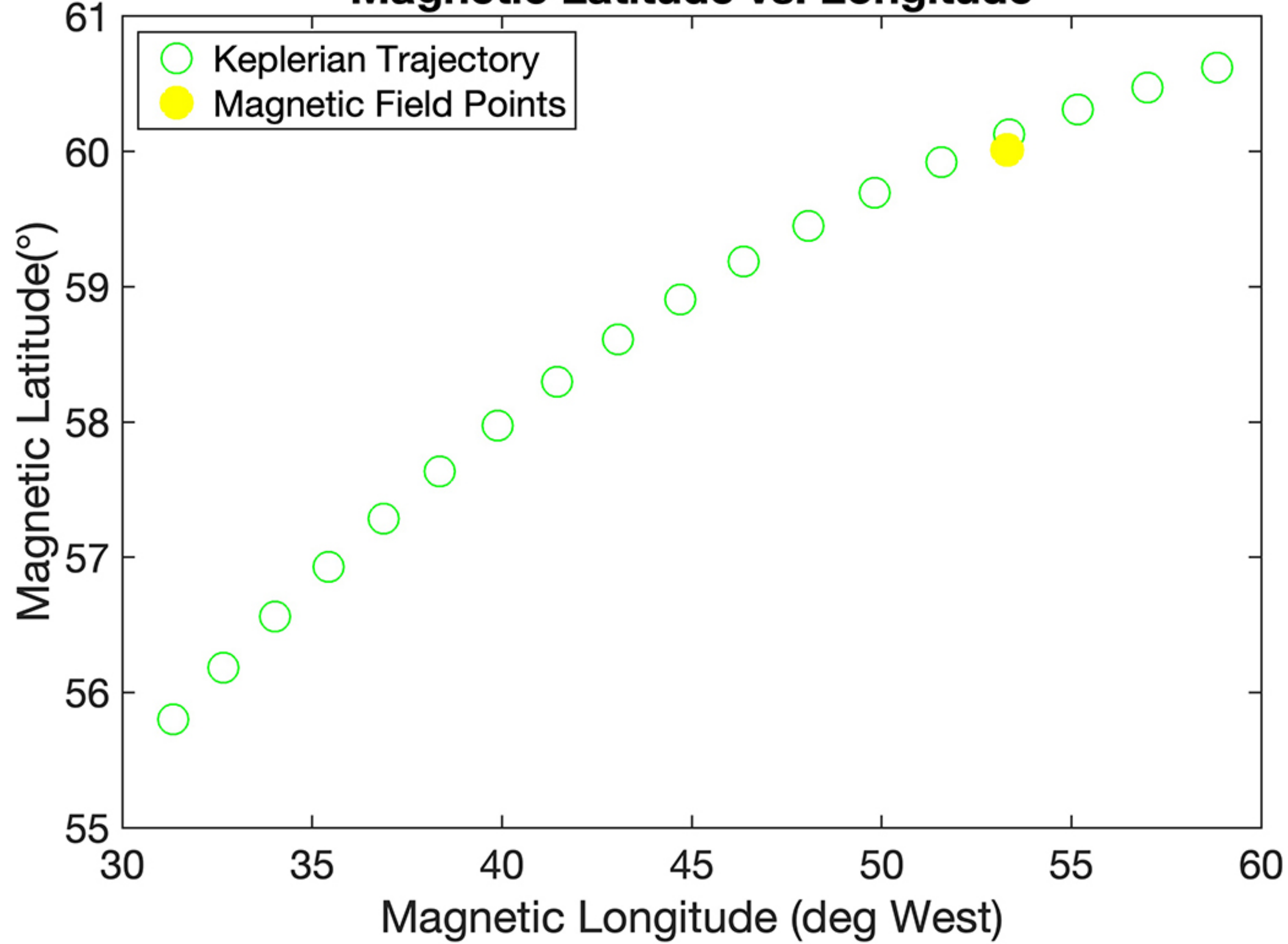
LUCK 05:46:32



REGI 05:48:09



Magnetic Latitude vs. Longitude



Altitude vs. Magnetic Longitude

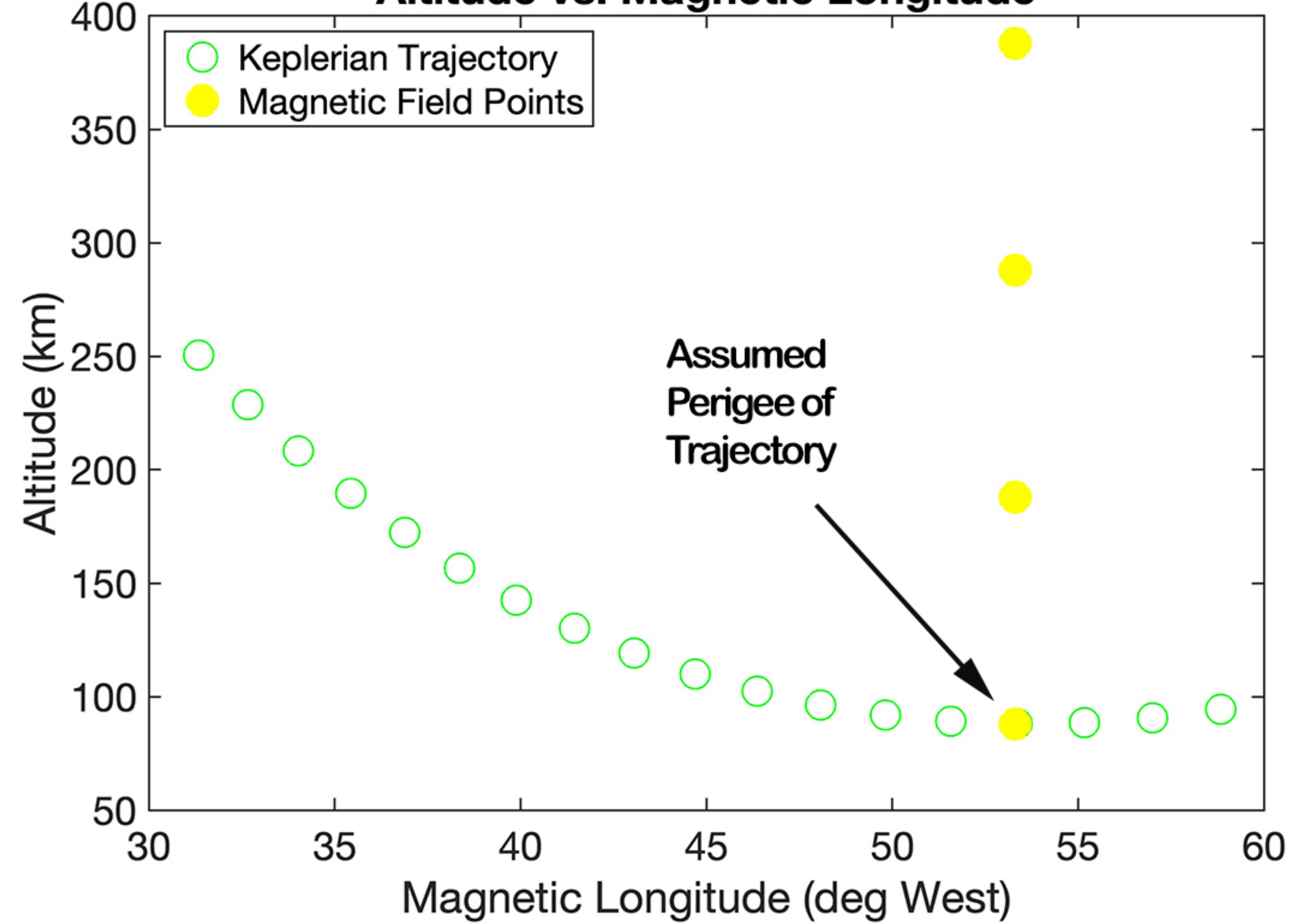
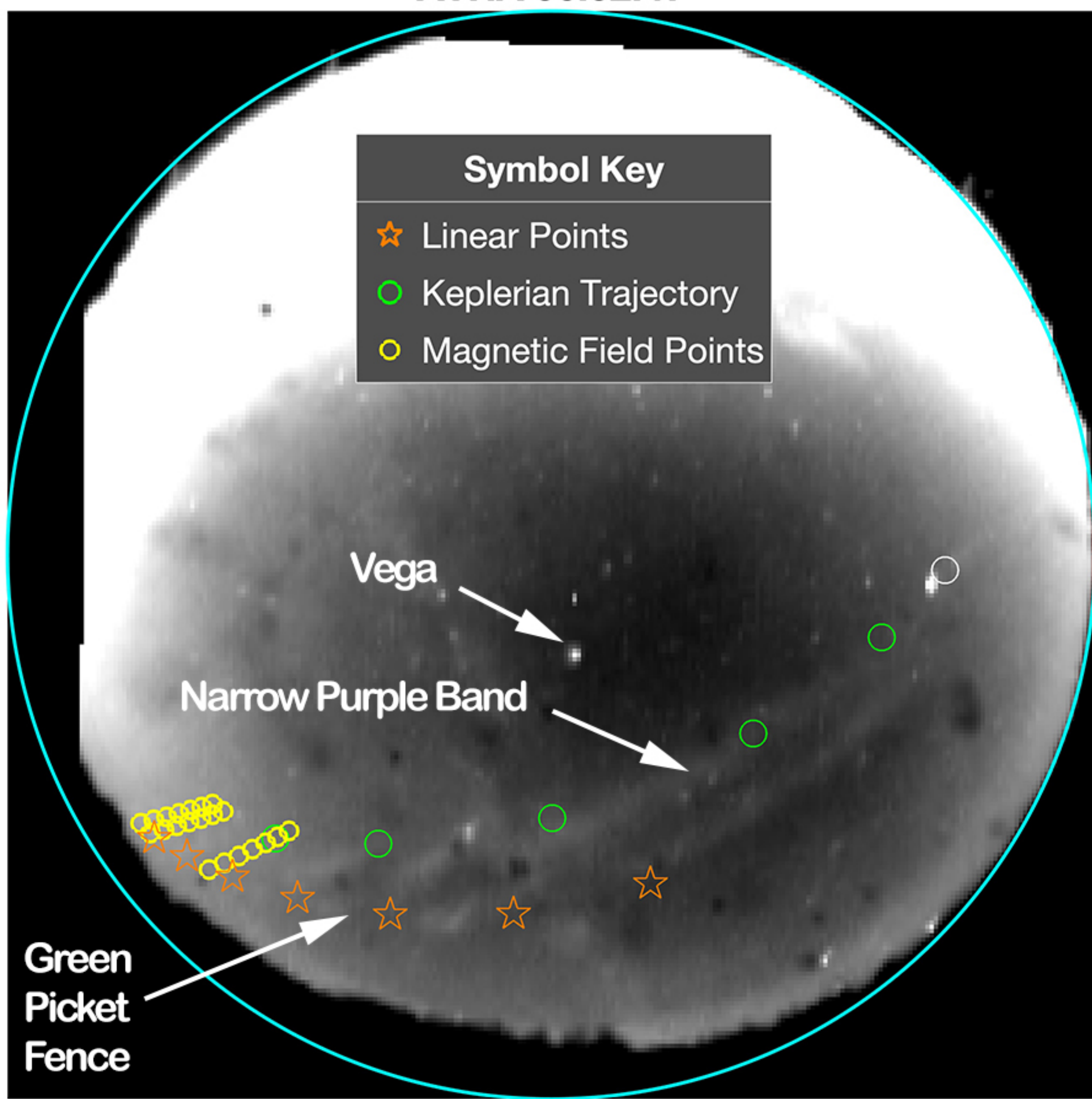
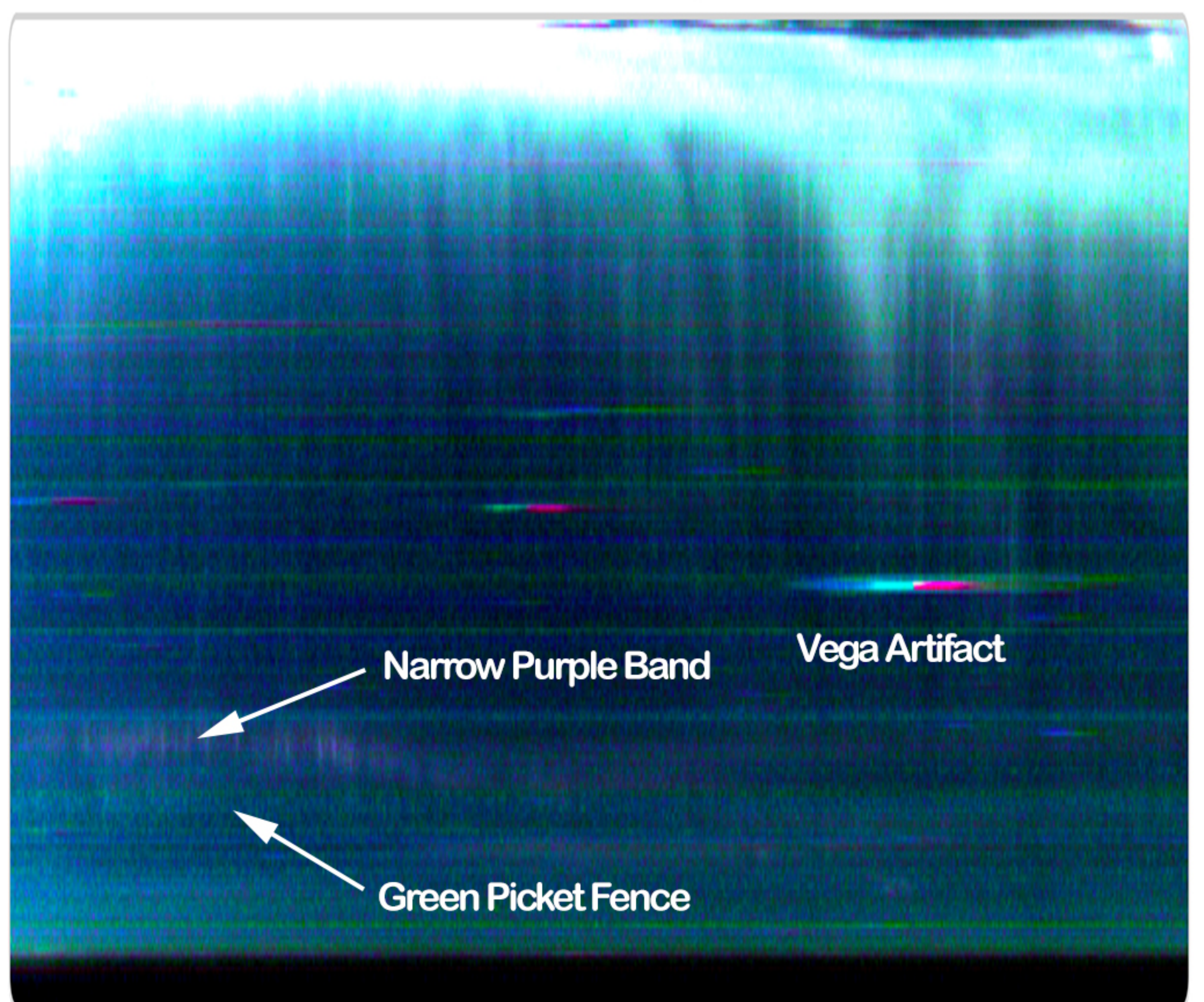


Figure 6.

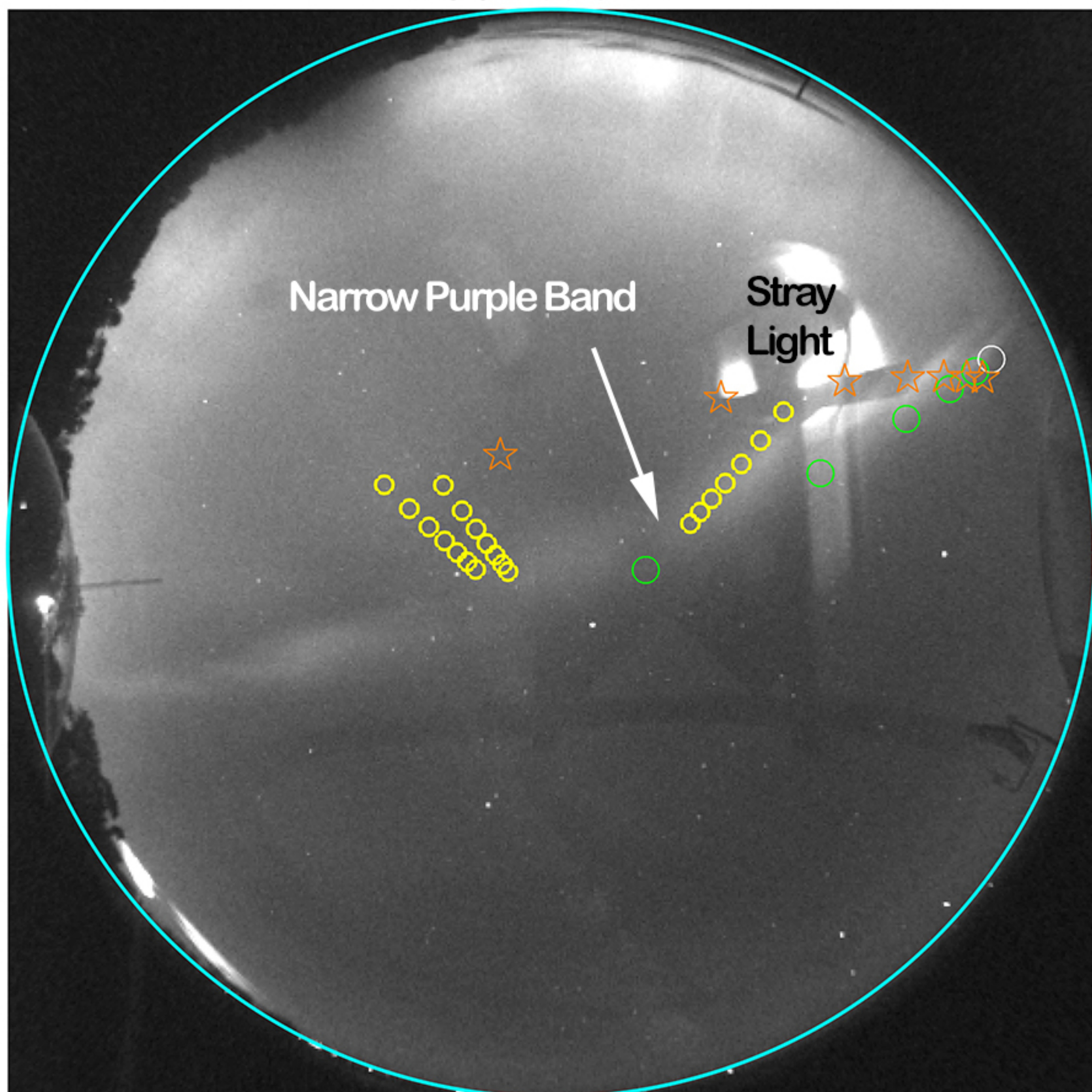
ATHA 06:02:47



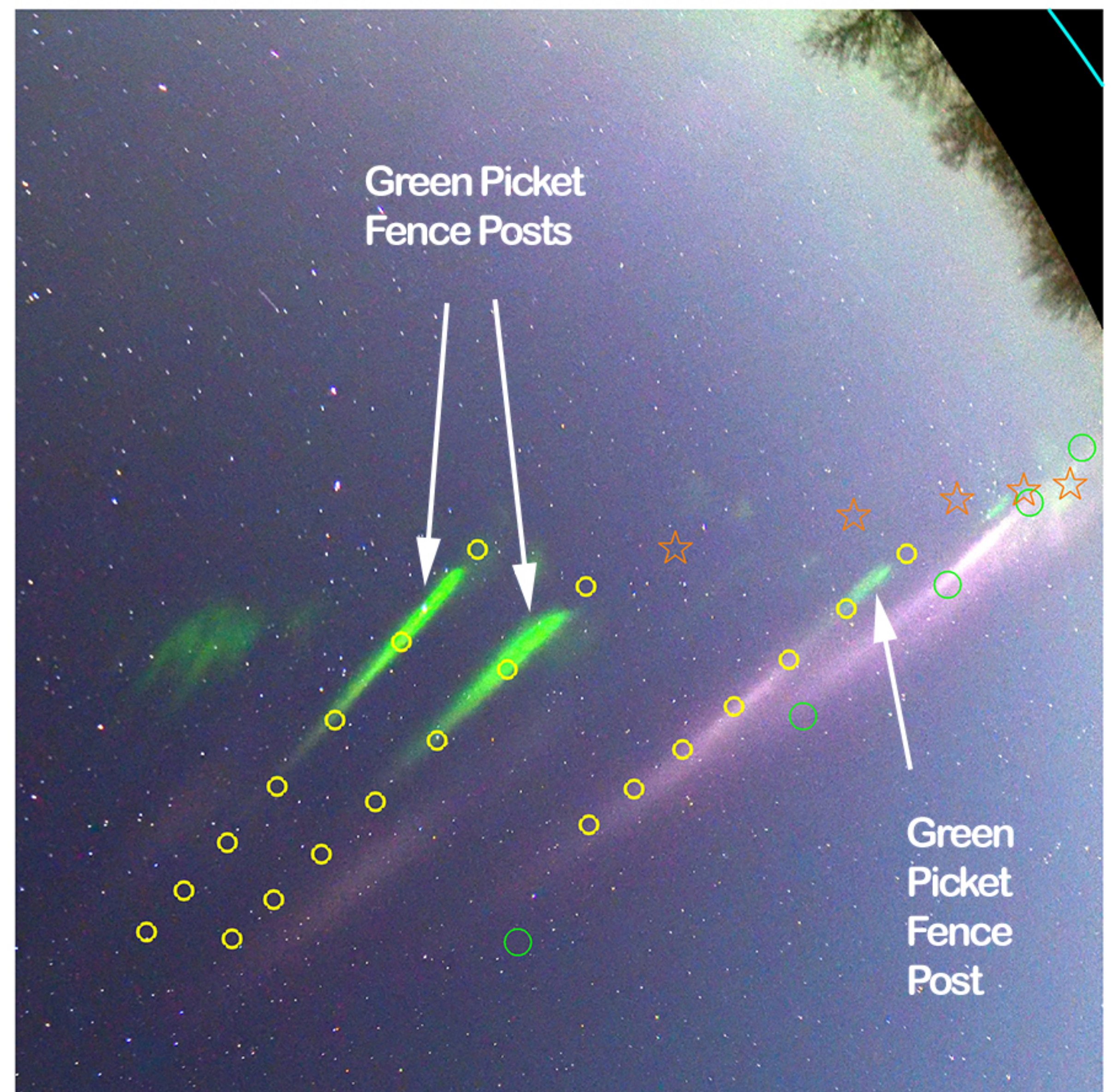
ATHA RAINBOW Keogram 6:00 - 6:59



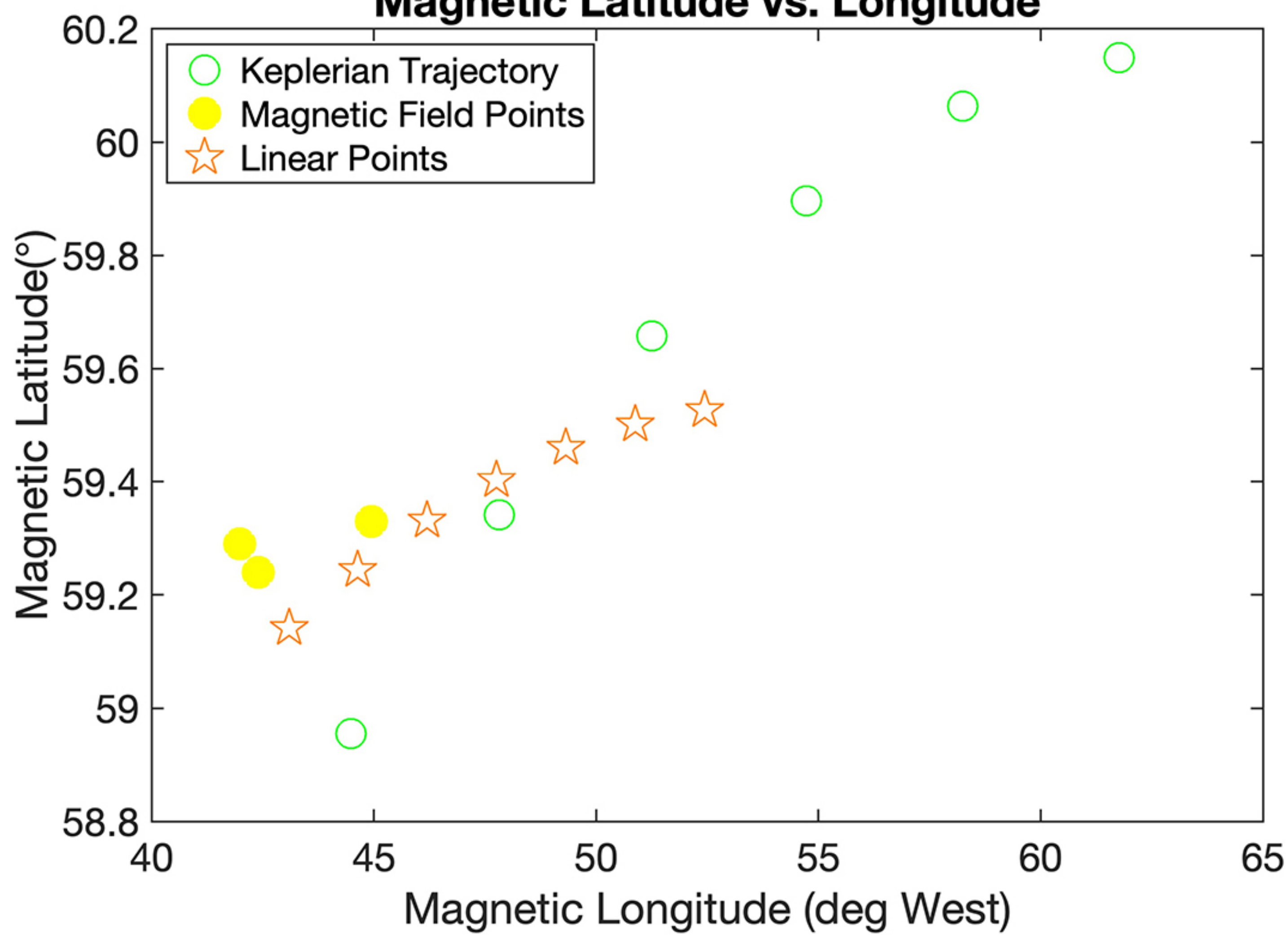
LUCK 06:02:47



REGI 06:02:48



Magnetic Latitude vs. Longitude



Altitude vs. Magnetic Longitude

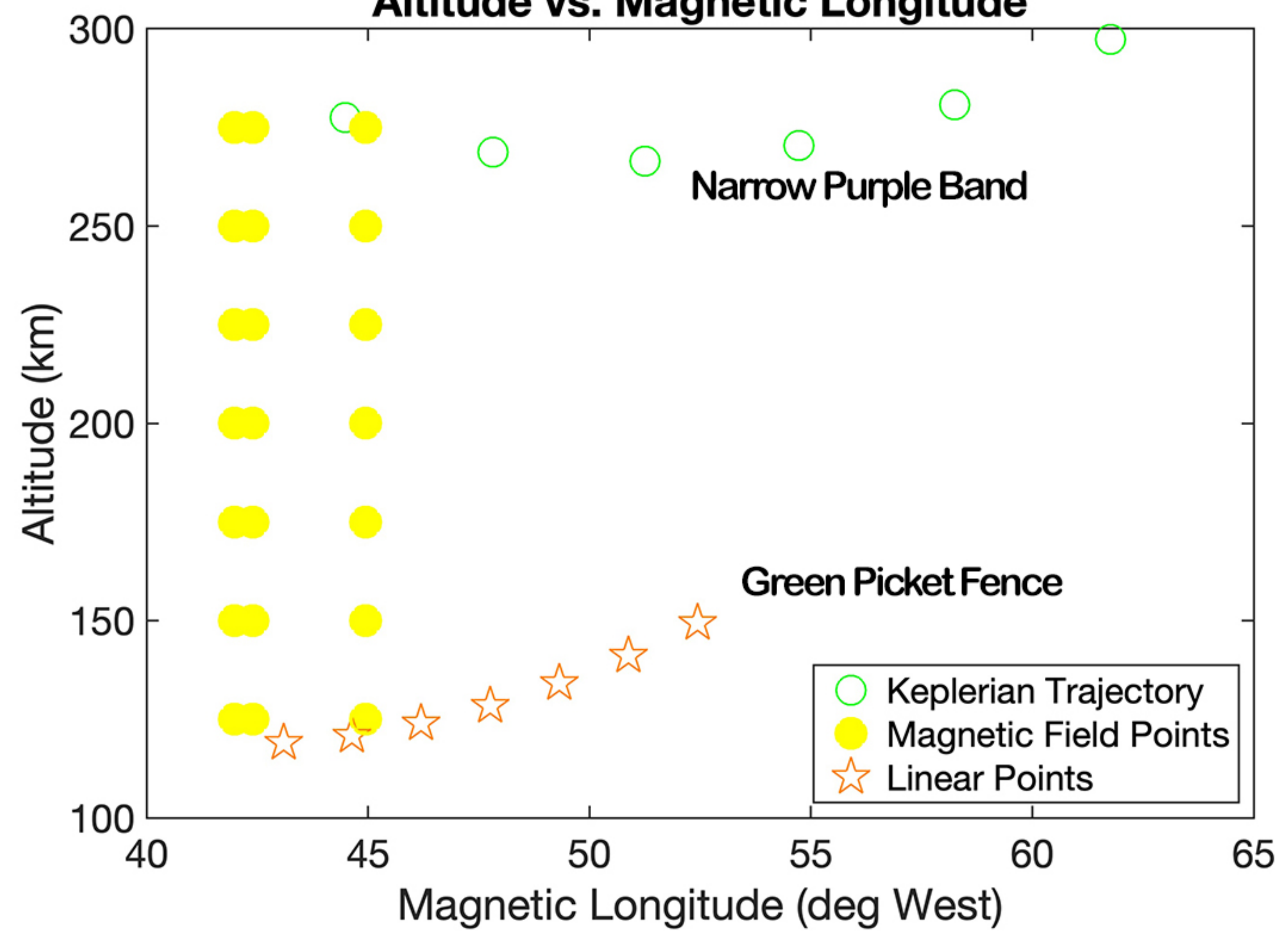
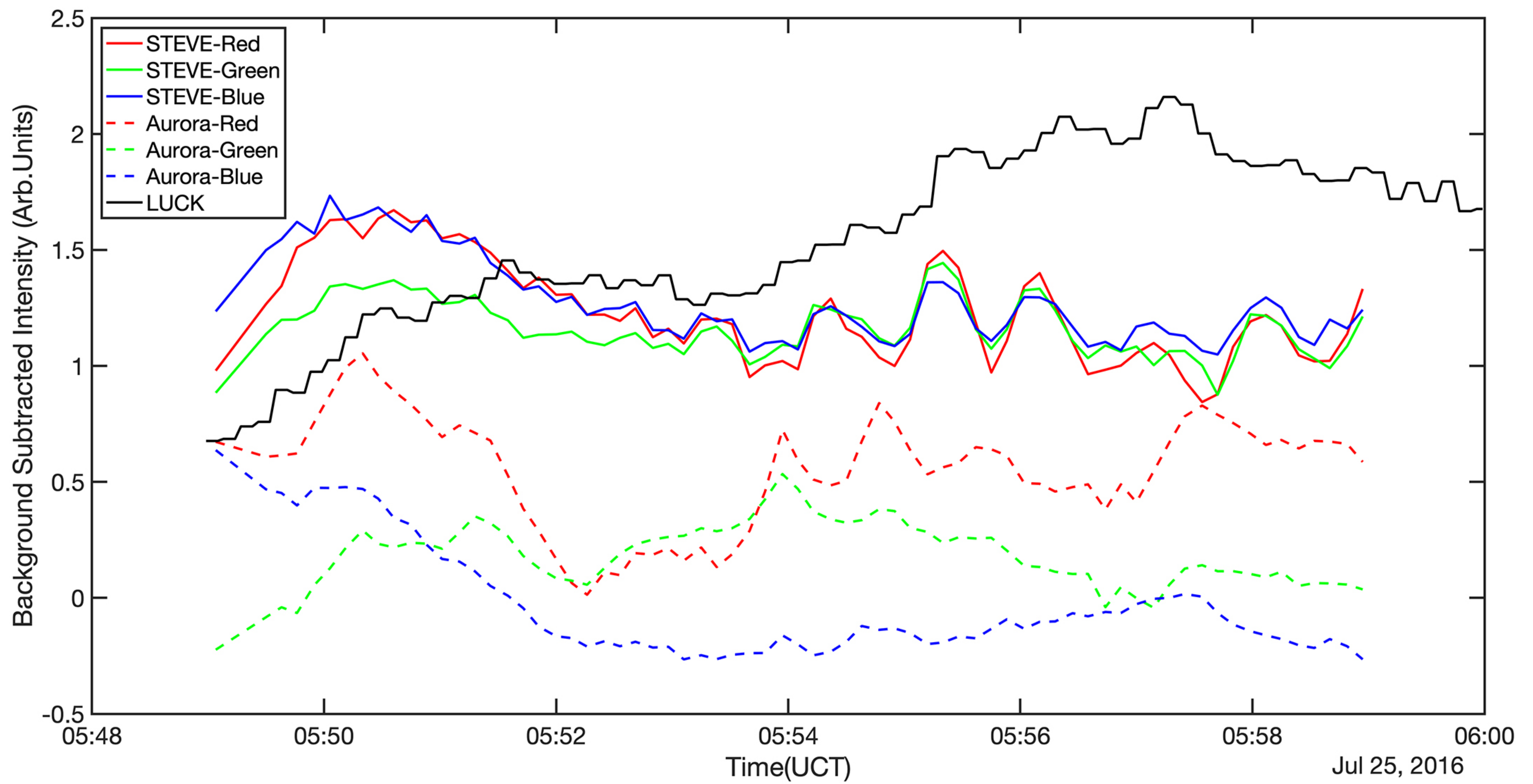
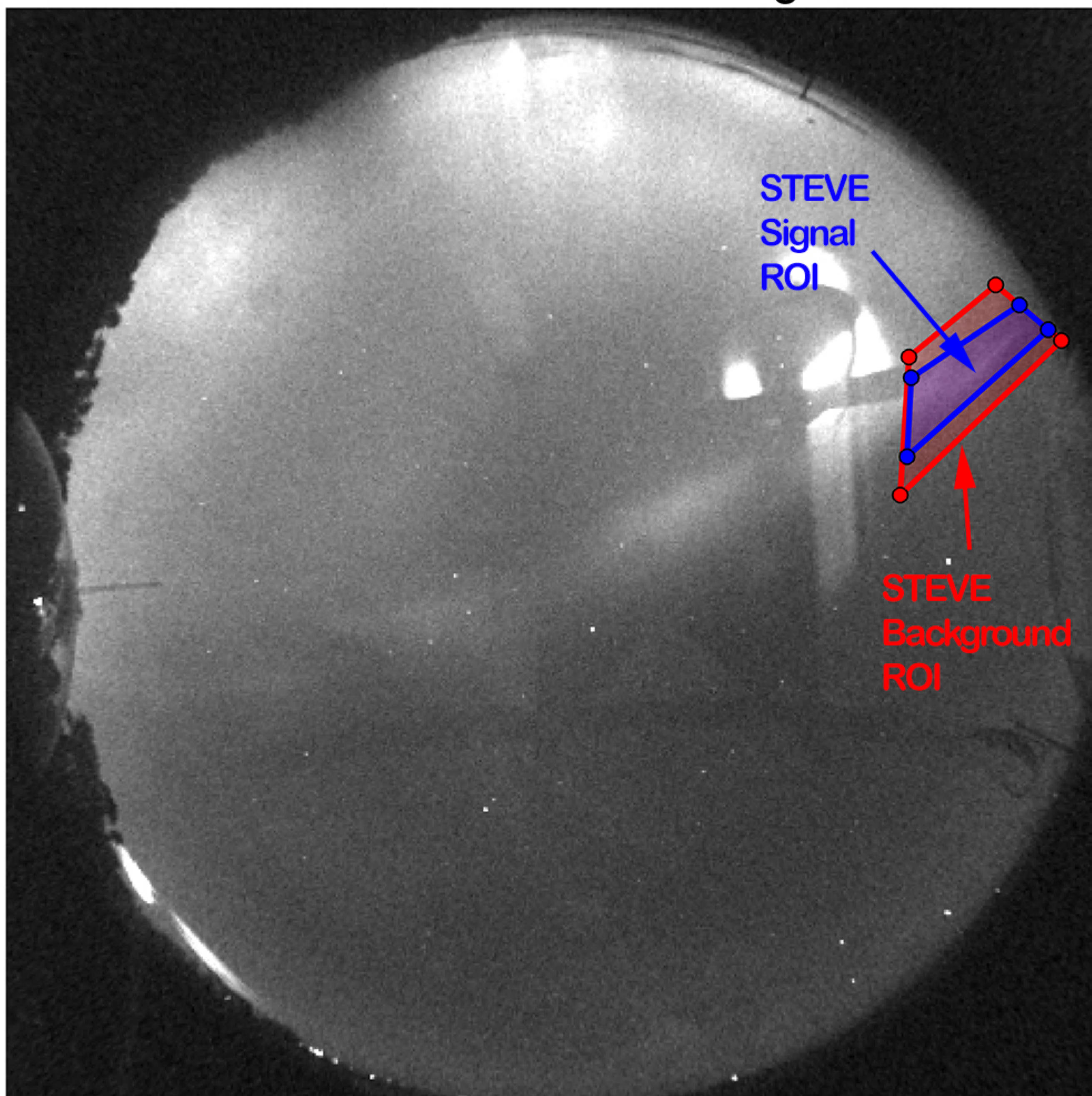


Figure 7.



LUCK ROI Selection Image



REGI ROI Selection Image

